

Uncertainty quantification for an optical grating coupler with an adjoint-based Leja adaptive collocation method

Niklas Georg^{a,b,c,*}, Dimitrios Loukrezis^{b,c}, Ulrich Römer^a, Sebastian Schöps^{b,c}

^a*Institute of Dynamics and Vibrations, Technische Universität Braunschweig, Germany*

^b*Centre for Computational Engineering, Technische Universität Darmstadt, Germany*

^c*Institut für Theorie Elektromagnetischer Felder, Technische Universität Darmstadt, Germany*

Abstract

This paper addresses uncertainties arising in the nano-scale fabrication of optical devices. The stochastic collocation method is used to propagate uncertainties in material and geometry to the scattering parameters of the system. A dimension-adaptive scheme based on Leja nodes is employed to reduce the computational complexity. By combining the Leja adaptive algorithm with an adjoint-based error indicator, an even smaller complexity is obtained. The scheme's efficiency is demonstrated by numerical results for an optical grating coupler. For this model problem, the adaptive strategy allows to compute statistical moments, probabilities and global sensitivity indices, taking into account a moderately high number of uncertain input parameters. In particular, it is found that geometric sensitivities outweigh sensitivities with respect to material parameters for the considered setting.

Keywords: adaptivity, adjoint error indicator, hierarchical interpolation, Maxwell's source problem, plasmonics, polynomial chaos

1. Introduction

Plasmonic structures offer great potential for subwavelength optics and optoelectronics [1] and have been intensively studied from both a fundamental and an application point of view in recent years. The key principle is the interaction of an optical excitation with surface plasmons on a metallic surface [2]. This interaction strongly depends on the subwavelength geometry [1], which can be suitably adjusted using modern nano-scale fabrication methods. A high coupling efficiency can be achieved, e.g. using grating couplers [3, 4, 5]. These structures can be analyzed using methods from computational electromagnetics [6], such as the rigorous coupled-wave analysis (RCWA) [7, 8], the finite-difference time-domain (FDTD) method [9, 10, 11], the boundary element method (BEM) [12, 13], continuous Galerkin methods in the frequency domain [14, 15] and the discontinuous Galerkin time-domain (DGTD) method [16, 17, 18, 19, 20].

Due to recent developments in uncertainty quantification (UQ) [21], studying statistical parameter variations within the numerical simulation of fields and waves comes into reach. Quantifying uncertainties for optical components and plasmonic structures in particular is highly desirable, as relatively large variabilities of nano-scale geometrical parameters can be observed, see, e.g. [5]. In addition, in view of the complicated measurement process, uncertainties are present in dispersion parameters or the dispersion model itself. Inferring parameter statistics from measurements and assessing model-form uncertainties are important tasks of current interest, but beyond the scope of this paper. Instead, we focus on the propagation of uncertainties from the model inputs to the outputs, in order to compute global sensitivities and confidence intervals for physical quantities of interest (QoIs).

In recent years, spectral methods for UQ have been developed as an efficient alternative to Monte Carlo simulation [21, 22, 23, 24, 25, 26]. These methods are continuously improved to address large-scale problems with many uncertain input parameters, which still pose a computational challenge nowadays. Adaptivity in combination with polynomial approximation is a promising technique to delay the curse-of-dimensionality. Other approaches rely on low-rank tensor decompositions [27], active subspaces [28] or model-order reduction [29, 30, 31], which however will not be

*Corresponding author: Tel.: +49-6151-1624393; fax: +49-6151-16-24404;
Email address: n.georg@tu-braunschweig.de (Niklas Georg)

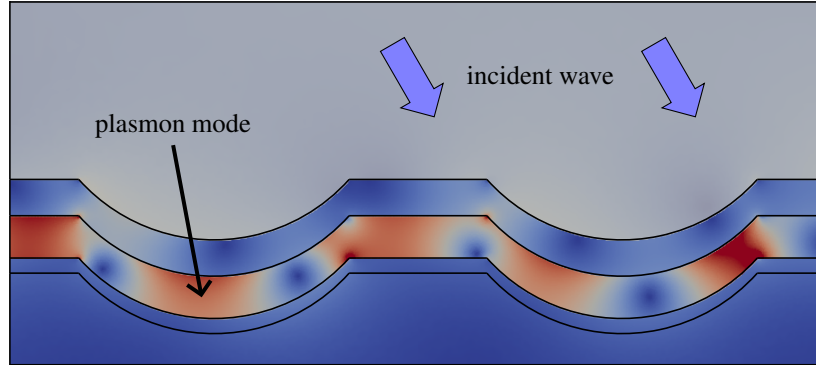


Figure 1: Optical coupling into MIM plasmon modes [5].

considered here. Spectral methods have been applied to a wide range of areas for UQ purposes, e.g. fluid dynamics [32, 33] and structural mechanics [34], to mention the most common ones. Wave propagation has been considered much later and it was observed that spectral methods may fail to converge exponentially in this case [35]. In microwave engineering, polynomial approximations have been applied in [36] for the case of low-dimensional uncertainty, while an academic, moderately high-dimensional example has been considered in [37]. Theoretical results for the Helmholtz transmission problem as a model for acoustic scattering and nano-optics have recently been obtained in [38, 39]. In those works, analytic regularity of the solution with respect to perturbations in the scatterer geometry was obtained for large wavelengths. The case of infinitely many input parameters was addressed by using an adaptive Smolyak algorithm, similar to the one presented in [40]. Based on the analyticity results, algebraic convergence rates, independent of the number of random inputs, were proven. As an alternative to polynomial methods, rational approximations of Padé-type have recently been employed for a Helmholtz problem with a random wave number [41].

In this paper, we present techniques to quantify uncertainties in subwavelength optical structures. As a model problem, we consider the optical coupling into metal-insulator-metal (MIM) plasmon modes with subwavelength diffraction gratings [5], which is illustrated in Fig. 1. A plane wave at optical frequency hits the surface of a grating coupler. The incident wave couples with a MIM plasmon mode, which propagates along the metallic surface. It is found that the MIM resonance has a significant shift (in energy) as a function of the grating depth [5] and therefore, it is of great interest to evaluate the influence of nano-technological manufacturing imperfections. Such a periodic structure can be addressed with FDTD, however, we use the finite element method (FEM), as it can easily handle complex geometries.

Both geometric and material parameters are modeled as random variables (RVs) and stochastic (pseudo)-spectral methods are used to compute moments, sensitivities and confidence intervals of the solution. We make use of polynomial surrogate modeling to compute the variability of the MIM resonance, by treating the excitation frequency as an additional parameter. We first recall well-established polynomial chaos techniques which are used for numerical comparisons, but also to numerically investigate the regularity of the considered output quantity based on the decay of coefficients. The main UQ technique in this work is an adaptive collocation method based on Leja points [40, 42], which is able to address the moderately high number of parameters in the considered model. In order to efficiently steer the adaptive selection of polynomials, we derive an adjoint representation of the stochastic error. Adjoint techniques have been used in a stochastic context before [43, 44], also in combination with Clenshaw-Curtis adaptive collocation [45, 46], and applied to a number of academic examples. In this work, we combine adjoint techniques with hierarchical Leja interpolation and apply the resulting scheme to a more complex model, i.e. an optical grating coupler. Contrary to the works [45, 46], the use of weighted Leja nodes allows us to consider non-uniformly distributed uncertain parameters. Results show clearly that the use of adjoint techniques improve the efficiency of adaptive collocation, also when the more “granular” Leja points are employed. We note that the methodologies for uncertainty analysis of the resonance frequency and adaptivity are presented and apply in a general context, although they are illustrated by means of an optical grating coupler.

The paper is structured as follows. In Section 2, the deterministic problem of wave scattering in periodic structures, its finite element discretization and its parametrization are presented. In Section 3 we introduce the UQ methods used for the simulation. We consider both generalized polynomial chaos (gPC) and adaptive interpolation based on Leja points. In this section we also introduce the adjoint error indicator and discuss the necessary adaptations to the adaptive algorithm. In Section 4, those UQ methods are applied to an optical grating coupler. After presenting the numerical

model and its parametrization, we first address the single-frequency case. We identify the most sensitive parameters and investigate the smoothness of the mapping from those inputs to the scattering parameter. Finally, we consider broadband calculations and perform UQ for the resonance. In the last section we give some concluding remarks.

2. Maxwell's Source Problem

In the following, we state Maxwell's source problem for the scattering in periodic structures with excitation by an incident plane wave. We also introduce the finite element (FE) discretization for the numerical approximation of fields and scattering parameters.

2.1. Deterministic Problem

We start with the time-harmonic Maxwell's equations,

$$\nabla \times \mathbf{E} = -j\omega\mu\mathbf{H} \quad \text{in } D, \quad (1a)$$

$$\nabla \times \mathbf{H} = \mathbf{J}_s + j\omega\epsilon\mathbf{E} \quad \text{in } D, \quad (1b)$$

$$\nabla \cdot (\epsilon\mathbf{E}) = \rho \quad \text{in } D, \quad (1c)$$

$$\nabla \cdot (\mu\mathbf{H}) = 0 \quad \text{in } D, \quad (1d)$$

where \mathbf{E} denotes the electric field phasor, \mathbf{H} the magnetic field phasor, \mathbf{J}_s the source current phasor, ρ the charge density phasor, ω the angular frequency, ϵ the dispersive complex permittivity, μ the permeability and D the computational domain to be specified. The permeability $\mu = \mu_0\mu_r$, where μ_r and μ_0 represent the relative and vacuum permeability, respectively, is assumed to be nondispersive. In absence of charges and source currents, i.e. $\rho = 0$ and $\mathbf{J}_s = 0$, the so-called curl-curl equation reads

$$\nabla \times (\mu_r^{-1} \nabla \times \mathbf{E}) - \omega^2 \epsilon \mu_0 \mathbf{E} = 0 \quad \text{in } D, \quad (2)$$

to be endowed with appropriate boundary conditions.

Given an infinitely periodic structure and a periodic excitation, the computational domain D can be confined to a single unit cell of the periodic structure, based on Floquet's Theorem [14, Chapter 13]. The unit cell is illustrated in Fig. 2. Without loss of generality we assume periodicity in the x and y directions, whereas Γ_{z^+} and Γ_{z^-} denote the

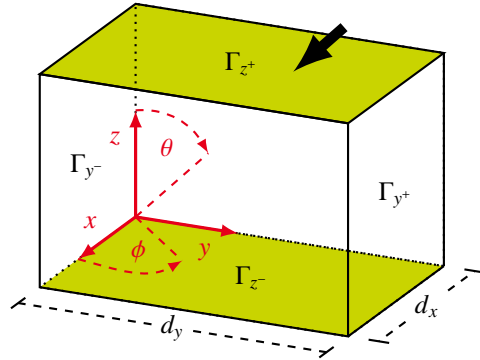


Figure 2: Sketch of a unit cell representing the computational domain D . The black arrow indicates the incident wavevector \mathbf{k}^{inc} .

boundaries in the non-periodic direction. At Γ_{z^+} the structure is excited by an incident plane wave

$$\mathbf{E}^{\text{inc}} = \mathbf{E}_0 e^{-j\mathbf{k}^{\text{inc}} \cdot \mathbf{r}}, \quad \mathbf{k}^{\text{inc}} = \begin{bmatrix} k_x^{\text{inc}} \\ k_y^{\text{inc}} \\ k_z^{\text{inc}} \end{bmatrix} = -k_0 \begin{bmatrix} \sin \theta^{\text{inc}} \cos \phi^{\text{inc}} \\ \sin \theta^{\text{inc}} \sin \phi^{\text{inc}} \\ \cos \theta^{\text{inc}} \end{bmatrix}, \quad (3)$$

where θ^{inc} , ϕ^{inc} are the angles of incidence and $k_0 = \omega \sqrt{\mu_0 \epsilon_0}$ the wavenumber in vacuum. It is worth noting that, due to the oblique angles, the periodicity of the excitation differs from the geometrical periodicity of the structure. According to Floquet's theorem, we need to enforce periodic phase-shift boundary conditions,

$$\mathbf{E}|_{\Gamma_{x^+}} = \mathbf{E}|_{\Gamma_{x^-}} e^{j\psi_x}, \quad \psi_x = -k_x^{\text{inc}} d_x \quad \text{on } \Gamma_{x^+} \cup \Gamma_{x^-}, \quad (4a)$$

$$\mathbf{E}|_{\Gamma_{y^+}} = \mathbf{E}|_{\Gamma_{y^-}} e^{j\psi_y}, \quad \psi_y = -k_y^{\text{inc}} d_y \quad \text{on } \Gamma_{y^+} \cup \Gamma_{y^-}, \quad (4b)$$

where the phase-shifts ψ_x, ψ_y depend only on the wavevector \mathbf{k}^{inc} of the incident wave at Γ_{z^+} and on the dimensions d_x, d_y of the unit cell.

To truncate the structure in the non-periodic direction at Γ_{z^+} , a Floquet absorbing boundary condition can be derived by splitting the electric field in the unbounded, homogeneous region $z \geq z^+$ as

$$\mathbf{E} = \mathbf{E}^{\text{inc}} + \mathbf{E}^{\text{sc}}, \quad (5)$$

where \mathbf{E}^{inc} and \mathbf{E}^{sc} represent the known incident field and the unknown scattered field, respectively. As derived in [47, Chapter 3] and [48, Chapter 12.2.1], the scattered field \mathbf{E}^{sc} can be represented as an infinite series of Floquet modes

$$\begin{aligned} \mathbf{E}^{\text{sc}} &= \sum_{\substack{m,n \in \mathbb{Z} \\ \alpha \in \{\text{TE}, \text{TM}\}}} c_{\alpha, mn} \mathbf{E}_{\alpha, mn} e^{-j\kappa_{mn}(z-z^+)}, \quad \text{where} \\ \mathbf{E}_{\text{TE}, mn} &:= \frac{e^{-j(k_{xm}x + k_{yn}y)}}{\sqrt{d_x d_y} \sqrt{k_{xm}^2 + k_{yn}^2}} (k_{yn} \mathbf{e}_x - k_{xm} \mathbf{e}_y), \\ \mathbf{E}_{\text{TM}, mn} &:= \frac{e^{-j(k_{xm}x + k_{yn}y)}}{\sqrt{d_x d_y} \sqrt{k_{xm}^2 + k_{yn}^2}} \left(k_{xm} \mathbf{e}_x + k_{yn} \mathbf{e}_y - \frac{k_{xm}^2 + k_{yn}^2}{\kappa_{mn}} \mathbf{e}_z \right), \\ \text{with } k_{xm} &:= k_x^{\text{inc}} + \frac{2\pi m}{d_x}, \quad k_{yn} := k_y^{\text{inc}} + \frac{2\pi n}{d_y}, \quad \kappa_{mn} := \sqrt{k_0^2 - k_{xm}^2 - k_{yn}^2}. \end{aligned} \quad (6)$$

Thereby, we distinguish between transverse electric (TE) modes $\mathbf{E}_{\text{TE}, mn}$ and transverse magnetic (TM) modes $\mathbf{E}_{\text{TM}, mn}$, fulfilling $\mathbf{E} \perp \mathbf{e}_z$ and $\mathbf{H} \perp \mathbf{e}_z$, respectively. There exists only a finite number of propagating modes, i.e. $\kappa_{mn} \in \mathbb{R}$, depending on the wavenumber k_0 , the angles of incidence $\theta^{\text{inc}}, \phi^{\text{inc}}$ and the dimensions d_x, d_y of the unit cell.

We introduce the operators $\pi_{\text{t}}[\mathbf{u}] := \mathbf{e}_z \times \mathbf{u}$ and $\pi_{\text{T}}[\mathbf{u}] := (\mathbf{e}_z \times \mathbf{u}) \times \mathbf{e}_z$ such that

$$\begin{aligned} \pi_{\text{t}}[\mathbf{H}_{\alpha, mn} e^{-j\kappa_{mn}(z-z^+)}] &= \pi_{\text{t}} \left[\frac{j}{\omega \mu} \nabla \times (\mathbf{E}_{\alpha, mn} e^{-j\kappa_{mn}(z-z^+)}) \right] \\ &= -Y_{\alpha, mn} \pi_{\text{T}}[\mathbf{E}_{\alpha, mn} e^{-j\kappa_{mn}(z-z^+)}], \\ \text{with } Y_{\alpha, mn} &:= \begin{cases} \frac{\kappa_{mn}}{\omega \mu} & \text{for } \alpha = \text{TE}, \\ \frac{\omega \epsilon}{\kappa_{mn}} & \text{for } \alpha = \text{TM}. \end{cases} \end{aligned} \quad (7)$$

The incident plane wave \mathbf{E}^{inc} corresponds to the lowest order Floquet modes $\mathbf{E}_{\alpha, 00}$ with modal admittance Y^{inc}

$$\pi_{\text{t}}[\mathbf{H}^{\text{inc}}] = Y^{\text{inc}} \pi_{\text{T}}[\mathbf{E}^{\text{inc}}], \quad Y^{\text{inc}} := \begin{cases} \frac{\sqrt{\epsilon} \cos(\theta^{\text{inc}})}{\sqrt{\mu}} & \text{for } \alpha = \text{TE}, \\ \frac{\sqrt{\epsilon}}{\sqrt{\mu} \cos(\theta^{\text{inc}})} & \text{for } \alpha = \text{TM}. \end{cases} \quad (8)$$

By taking the cross product of the curl of (5) with \mathbf{e}_z , the magnetic field above the structure is expressed as

$$\pi_{\text{t}}[\mathbf{H}] + \sum_{\substack{m,n \in \mathbb{Z} \\ \alpha \in \{\text{TE}, \text{TM}\}}} \tilde{c}_{\alpha, mn} Y_{\alpha, mn} \pi_{\text{T}}[\mathbf{E}_{\alpha, mn} e^{-j\kappa_{mn}(z-z^+)}] = 2Y^{\text{inc}} \pi_{\text{T}}[\mathbf{E}^{\text{inc}}]. \quad (9)$$

For any $\mathbf{u}, \mathbf{v} \in (L^2(\Gamma_{z^+}))^3$, the space of square-integrable complex vector functions on Γ_{z^+} , we introduce the inner product

$$(\mathbf{u}, \mathbf{v})_{\Gamma_{z^+}} := \int_{\Gamma_{z^+}} \mathbf{u} \cdot \mathbf{v}^* \, \text{d}\mathbf{x}, \quad (10)$$

where the superscript $*$ denotes complex conjugation. Due to the orthogonality of the modal basis, i.e.

$$\left(\pi_{\text{T}}[\mathbf{E}_{\text{TE}, mn}], \pi_{\text{T}}[\mathbf{E}_{\text{TE}, ij}] \right)_{\Gamma_{z^+}} = \left(\pi_{\text{T}}[\mathbf{E}_{\text{TM}, mn}], \pi_{\text{T}}[\mathbf{E}_{\text{TM}, ij}] \right)_{\Gamma_{z^+}} = \delta_{mi} \delta_{nj}, \quad (11a)$$

$$\left(\pi_{\text{T}}[\mathbf{E}_{\text{TE}, mn}], \pi_{\text{T}}[\mathbf{E}_{\text{TM}, ij}] \right)_{\Gamma_{z^+}} = 0, \quad (11b)$$

where δ denotes the Kronecker delta, the unknown coefficients $\tilde{c}_{\alpha, mn} \in \mathbb{C}$ of the modal expansion (9) can be obtained as

$$\begin{aligned}\tilde{c}_{\alpha, mn} &= (\pi_{\mathbf{T}}[\mathbf{E}], \pi_{\mathbf{T}}[\mathbf{E}_{\alpha, mn}])_{\Gamma_{z^+}} \\ &= \underbrace{(\pi_{\mathbf{T}}[\mathbf{E}^{\text{sc}}], \pi_{\mathbf{T}}[\mathbf{E}_{\alpha, mn}])_{\Gamma_{z^+}}}_{=c_{\alpha, mn}} + (\pi_{\mathbf{T}}[\mathbf{E}^{\text{inc}}], \pi_{\mathbf{T}}[\mathbf{E}_{\alpha, mn}])_{\Gamma_{z^+}}.\end{aligned}\quad (12)$$

Equation (9) represents the boundary condition to be imposed on Γ_{z^+} . In practice, the infinite sum of Floquet modes is truncated to $-m_{\max} \leq m \leq m_{\max}$, $-n_{\max} \leq n \leq n_{\max}$. Further simplifications are possible if the dimensions of the unit cell are small enough, such that only the fundamental modes $\mathbf{E}_{\alpha, 00}$ propagate, and the boundary Γ_{z^+} is placed sufficiently far away from the structure, such that all higher order modes are attenuated to a negligible amplitude. In this case, the fundamental mode is of particular interest and we may omit all evanescent higher order modes. In particular, we can employ the first-order absorbing boundary condition [14, Chapter 13.4.1], i.e.

$$\pi_{\mathbf{t}}[\mathbf{H}] - \frac{\mathbf{k}_{\mathbf{t}}^{\text{inc}}}{\omega\mu k_z^{\text{inc}}} (\mathbf{k}_{\mathbf{t}}^{\text{inc}} \cdot \pi_{\mathbf{T}}[\mathbf{E}]) - \frac{k_z^{\text{inc}}}{\omega\mu} \pi_{\mathbf{T}}[\mathbf{E}] = 2Y^{\text{inc}} \pi_{\mathbf{T}}[\mathbf{E}^{\text{inc}}], \quad \text{where } \mathbf{k}_{\mathbf{t}}^{\text{inc}} := \pi_{\mathbf{T}}[\mathbf{k}^{\text{inc}}]. \quad (13)$$

At Γ_{z^-} , a perfect electric conductor (PEC) boundary condition is applied to truncate the structure, i.e.

$$\mathbf{n} \times \mathbf{E} = 0 \quad \text{on } \Gamma_{z^-}, \quad (14)$$

however, different boundary conditions are also possible, e.g. again a Floquet absorbing boundary condition or perfectly matched layers (PML) [14].

In summary, we are concerned with the boundary value problem

$$\nabla \times (\mu_{\mathbf{r}}^{-1} \nabla \times \mathbf{E}) - \omega^2 \epsilon \mu_0 \mathbf{E} = 0 \quad \text{in } D, \quad (15a)$$

$$\mathbf{E}|_{\Gamma_{x^+}} = \mathbf{E}|_{\Gamma_{x^-}} e^{j\psi_x} \quad \text{on } \Gamma_{x^+} \cup \Gamma_{x^-}, \quad (15b)$$

$$\mathbf{E}|_{\Gamma_{y^+}} = \mathbf{E}|_{\Gamma_{y^-}} e^{j\psi_y} \quad \text{on } \Gamma_{y^+} \cup \Gamma_{y^-}, \quad (15c)$$

$$\mathbf{n} \times \mathbf{E} = 0 \quad \text{on } \Gamma_{z^-}, \quad (15d)$$

$$\pi_{\mathbf{t}}[\mathbf{H}] + \sum_{\substack{|m| \leq m_{\max} \\ |n| \leq n_{\max} \\ \alpha \in \{\text{TE}, \text{TM}\}}} \tilde{c}_{\alpha, mn} Y_{\alpha, mn} \pi_{\mathbf{T}}[\mathbf{E}_{\alpha, mn}] = 2Y^{\text{inc}} \pi_{\mathbf{T}}[\mathbf{E}^{\text{inc}}] \quad \text{on } \Gamma_{z^+}. \quad (15e)$$

2.1.1. Weak formulation and discretization

To simplify the notation, we introduce the traces

$$\mathbf{u}_{\mathbf{T}} := (\mathbf{n}_{\Gamma} \times \mathbf{u}|_{\Gamma}) \times \mathbf{n}_{\Gamma}, \quad (16a)$$

$$\mathbf{u}_{\mathbf{t}} := \mathbf{n}_{\Gamma} \times \mathbf{u}|_{\Gamma}, \quad (16b)$$

where $\Gamma := \partial D$ denotes the boundary of D and \mathbf{n}_{Γ} refers to its outer unit normal.

By building the inner product of (15a) with tests function $\mathbf{E}' \in V$, where V is to be determined, and integration by parts we obtain

$$(\mu_{\mathbf{r}}^{-1} \nabla \times \mathbf{E}, \nabla \times \mathbf{E}')_D - \omega^2 \mu_0 (\epsilon \mathbf{E}, \mathbf{E}')_D - j\omega \mu_0 (\mathbf{H}_{\mathbf{t}}, \mathbf{E}'_{\mathbf{T}})_{\Gamma} = 0. \quad (17)$$

The boundary integral can be further simplified, i.e. the contributions on Γ_{x^+} , Γ_{x^-} and Γ_{y^+} , Γ_{y^-} cancel each other due to the periodic phase-shift boundary conditions (15b), (15c) of trial and test functions. We further eliminate the portion of the integral on Γ_{z^-} by demanding that the test functions \mathbf{E}' fulfill the PEC boundary condition (15d).

The appropriate function space V for a weak formulation is a subspace of $\mathbf{H}(\text{curl}; D)$, i.e. the (complex) vector function space of square-integrable functions with square-integrable curl. For more details on function spaces in the context of Maxwell's source problem, the reader is referred to [15, Chapter 3]. To account for the boundary conditions in (15), the function space is chosen as

$$\begin{aligned}V := \{ \mathbf{v} \in \mathbf{H}(\text{curl}; D) : \mathbf{v}_{\mathbf{T}}|_{\Gamma_{z^-}} = 0 \wedge \mathbf{v}_{\mathbf{T}}|_{\Gamma_{x^+}} = -\mathbf{v}_{\mathbf{T}}|_{\Gamma_{x^-}} e^{j\psi_x} \wedge \\ \mathbf{v}_{\mathbf{T}}|_{\Gamma_{y^+}} = -\mathbf{v}_{\mathbf{T}}|_{\Gamma_{y^-}} e^{j\psi_y} \wedge \mathbf{v}_{\mathbf{T}}|_{\Gamma_{z^+}} \in (L^2(\Gamma_{z^+}))^3 \},\end{aligned}\quad (18)$$

where the condition $\mathbf{v}_T|_{\Gamma_{z^+}} \in (L^2(\Gamma_{z^+}))^3$ is required to obtain a well-defined boundary integral. The weak formulation reads: find $\mathbf{E} \in V$ s.t.

$$\left(\mu_r^{-1} \nabla \times \mathbf{E}, \nabla \times \mathbf{E}'\right)_D - \omega^2 \mu_0 (\epsilon \mathbf{E}, \mathbf{E}')_D - j\omega \mu_0 (\mathbf{H}_t, \mathbf{E}'_T)_{\Gamma_{z^+}} = 0 \quad \forall \mathbf{E}' \in V. \quad (19)$$

On Γ_{z^+} the Floquet absorbing boundary condition can be employed, leading to the variational formulation: find $\mathbf{E} \in V$ s.t.

$$a(\mathbf{E}, \mathbf{E}') = l(\mathbf{E}') \quad \forall \mathbf{E}' \in V, \quad (20)$$

where

$$a(\mathbf{E}, \mathbf{E}') := \left(\mu_r^{-1} \nabla \times \mathbf{E}, \nabla \times \mathbf{E}'\right)_\Omega - \omega^2 \mu_0 (\epsilon \mathbf{E}, \mathbf{E}')_\Omega + j\omega \mu_0 \sum_{\alpha, m, n} Y_{\alpha, mn} (\mathbf{E}_T, \pi_T [\mathbf{E}_{\alpha, mn}])_{\Gamma_{z^+}} (\pi_T [\mathbf{E}_{\alpha, mn}], \mathbf{E}'_T)_{\Gamma_{z^+}} \quad (21)$$

$$l(\mathbf{E}') := 2j\omega \mu_0 Y^{\text{inc}} (\mathbf{E}'_T, \mathbf{E}'_T)_{\Gamma_{z^+}}. \quad (22)$$

If the first-order Floquet boundary condition (13) is sufficient, $a(\cdot, \cdot)$ simplifies to

$$a^{\text{FO}}(\mathbf{E}, \mathbf{E}') := \left(\mu_r^{-1} \nabla \times \mathbf{E}, \nabla \times \mathbf{E}'\right)_D - \omega^2 \mu_0 (\epsilon \mathbf{E}, \mathbf{E}')_D - \frac{j}{k_z^{\text{inc}}} (\mathbf{k}_t^{\text{inc}} \cdot \mathbf{E}_T, \mathbf{k}_t^{\text{inc}} \cdot \mathbf{E}'_T)_{\Gamma_{z^+}} - jk_z^{\text{inc}} (\mathbf{E}_T, \mathbf{E}'_T)_{\Gamma_{z^+}}. \quad (23)$$

To ensure a curl-conforming discretization of (19), we approximate the electric field \mathbf{E} numerically as

$$\mathbf{E}_h(\mathbf{x}) = \sum_{j=1}^{N_h} c_j \mathbf{N}_j(\mathbf{x}) \quad (24)$$

where \mathbf{N}_j denotes Nédélec basis functions of the first kind [49, 15] and 1st or 2nd order, defined on a tetrahedral mesh of the domain D . The mesh is assumed to be periodic, i.e. the surface meshes on Γ_{x^+} and Γ_{x^-} , as well as on Γ_{y^+} and Γ_{y^-} , are respectively identical. Without loss of generality we further assume the vector of coefficients $\mathbf{c} \in \mathbb{C}^{N_h}$ to be ordered such that the boundary conditions imposed in (18) can be expressed as

$$\mathbf{c} = \begin{bmatrix} \mathbf{c}_{\text{inner}} \\ \mathbf{c}_{\Gamma_{z^+}} \\ \mathbf{c}_{\Gamma_{z^-}} \\ \mathbf{c}_{\Gamma_{x^+}} \\ \mathbf{c}_{\Gamma_{x^-}} \\ \mathbf{c}_{\Gamma_{y^+}} \\ \mathbf{c}_{\Gamma_{y^-}} \\ \mathbf{c}_{\Gamma_{x^+} \cap \Gamma_{y^+}} \\ \mathbf{c}_{\Gamma_{x^-} \cap \Gamma_{y^+}} \\ \mathbf{c}_{\Gamma_{x^+} \cap \Gamma_{y^-}} \\ \mathbf{c}_{\Gamma_{x^-} \cap \Gamma_{y^-}} \end{bmatrix} = \begin{bmatrix} \mathbf{I} & 0 & 0 & 0 & 0 \\ 0 & \mathbf{I} & 0 & 0 & 0 \\ 0 & 0 & 0 & 0 & 0 \\ 0 & 0 & \mathbf{I} & 0 & 0 \\ 0 & 0 & \mathbf{I} e^{-j\psi_x} & 0 & 0 \\ 0 & 0 & 0 & \mathbf{I} & 0 \\ 0 & 0 & 0 & \mathbf{I} e^{-j\psi_y} & 0 \\ 0 & 0 & 0 & 0 & \mathbf{I} \\ 0 & 0 & 0 & 0 & \mathbf{I} e^{-j\psi_x} \\ 0 & 0 & 0 & 0 & \mathbf{I} e^{-j\psi_y} \\ 0 & 0 & 0 & 0 & \mathbf{I} e^{-j(\psi_x + \psi_y)} \end{bmatrix} \begin{bmatrix} \mathbf{c}_{\text{inner}} \\ \mathbf{c}_{\Gamma_{z^+}} \\ \mathbf{c}_{\Gamma_{x^+}} \\ \mathbf{c}_{\Gamma_{y^+}} \\ \mathbf{c}_{\Gamma_{x^+} \cap \Gamma_{y^+}} \end{bmatrix} = \mathbf{P} \mathbf{c}_{\text{dof}},$$

where we have introduced the reduced vector $\mathbf{c}_{\text{dof}} \in \mathbb{C}^{N_{\text{DoF}}}$ of $N_{\text{DoF}} < N_h$ degrees of freedom (DoF) and \mathbf{I} denotes an identity matrix of appropriate size [14, Chapter 13.1.2].

Let $\mathbf{A} \in \mathbb{C}^{N_h \times N_h}$ and $\mathbf{f} \in \mathbb{C}^{N_h}$ be the system matrix and right-hand side vector, which are obtained by using (24) in (21) or (23) and (22), as well as Nédélec test functions. In case of using the higher-order Floquet port boundary condition, the boundary integrals of (21) lead to dense sub-blocks in the matrix \mathbf{A} , whereas (23) preserves the sparsity of the FE matrix. The quasi-periodic and PEC boundary conditions (18) on ansatz and test functions can be imposed conveniently using the matrix $\mathbf{P} \in \mathbb{C}^{N_h \times N_{\text{DoF}}}$, leading to the reduced system

$$\mathbf{A}_{\text{dof}} = \mathbf{P}^H \mathbf{A} \mathbf{P} \mathbf{c}_{\text{dof}} = \mathbf{P}^H \mathbf{f} = \mathbf{f}_{\text{dof}}, \quad (25)$$

where \mathbf{P}^H denotes the Hermitian transpose of \mathbf{P} . Functions spanned by the reduced DoF form a proper subspace of (18).

In practice, one is often interested in reflection and transmission coefficients, in addition to the field solution \mathbf{E} itself. Therefore, we define the scattering parameters

$$S_{mn}^{\text{TE}} := c_{\text{TE},mn} = \left(\mathbf{E}_T - \mathbf{E}_T^{\text{inc}}, \pi_T [\mathbf{E}_{\text{TE},mn}] \right)_{\Gamma_{z^+}}, \quad (26a)$$

$$S_{mn}^{\text{TM}} := c_{\text{TM},mn} = \left(\mathbf{E}_T - \mathbf{E}_T^{\text{inc}}, \pi_T [\mathbf{E}_{\text{TM},mn}] \right)_{\Gamma_{z^+}}, \quad (26b)$$

as (affine-)linear functionals of \mathbf{E} .

2.2. Parametrized model

In this subsection we specify the material distribution of the complex permittivity ϵ . In particular, we assume a linear material behaviour for ϵ and μ inside D . Let the domain D be composed of M non-overlapping subdomains D_m , i.e. $\bar{D} = \bigcup_{m=1}^M \bar{D}_m$. We further assume that the dispersive permittivity $\epsilon(\mathbf{x}, \omega)$ is spatially piecewise constant on each subdomain D_m and depends smoothly on a given vector of N parameters $\mathbf{y} \in \Xi \subset \mathbb{R}^N$

$$\epsilon(\mathbf{x}, \omega, \mathbf{y}) = \sum_{m=1}^M \epsilon_m(\omega, \mathbf{y}) \mathbb{1}_m(\mathbf{x}, \mathbf{y}), \quad \text{where} \quad \mathbb{1}_m(\mathbf{x}, \mathbf{y}) = \begin{cases} 1, & \mathbf{x} \in D_m(\mathbf{y}), \\ 0, & \mathbf{x} \notin D_m(\mathbf{y}). \end{cases} \quad (27)$$

On the one hand, the parameter vector \mathbf{y} can be used to represent variations in the material parameters, e.g. different permittivities, refractive indices or extinction coefficients, by changing the coefficients $\epsilon_m(\omega, \mathbf{y})$. On the other hand, it also represents geometric variations of the structure inside the unit cell, since the subdomains $D_m(\mathbf{y})$ for each material depend on \mathbf{y} as well.

The parametrized weak formulation reads: find $\mathbf{E}(\mathbf{y}) \in V$ s.t.

$$a_{\mathbf{y}}(\mathbf{E}(\mathbf{y}), \mathbf{E}') = l(\mathbf{E}') \quad \forall \mathbf{E}' \in V, \quad (28)$$

where

$$\begin{aligned} a_{\mathbf{y}}(\mathbf{E}, \mathbf{E}') &:= \left(\mu_r^{-1} \nabla \times \mathbf{E}(\mathbf{y}), \nabla \times \mathbf{E}' \right)_{\Omega} - \omega^2 \mu_0 (\epsilon(\mathbf{y}) \mathbf{E}(\mathbf{y}), \mathbf{E}')_{\Omega} \\ &\quad + j\omega \mu_0 \sum_{\alpha, m, n} Y_{\alpha, mn} (\mathbf{E}_T(\mathbf{y}), \pi_T [\mathbf{E}_{\alpha, mn}])_{\Gamma_{z^+}} (\pi_T [\mathbf{E}_{\alpha, mn}], \mathbf{E}'_T)_{\Gamma_{z^+}} \end{aligned} \quad (29)$$

for (9), and

$$\begin{aligned} a_{\mathbf{y}}^{\text{FO}}(\mathbf{E}, \mathbf{E}') &:= \left(\mu_r^{-1} \nabla \times \mathbf{E}(\mathbf{y}), \nabla \times \mathbf{E}' \right)_{\Omega} - \omega^2 \mu_0 (\epsilon(\mathbf{y}) \mathbf{E}(\mathbf{y}), \mathbf{E}')_{\Omega} \\ &\quad - \frac{j}{k_z^{\text{inc}}} \left(\mathbf{k}_t^{\text{inc}} \cdot \mathbf{E}_T(\mathbf{y}), \mathbf{k}_t^{\text{inc}} \cdot \mathbf{E}'_T \right)_{\Gamma_{z^+}} - j k_z^{\text{inc}} (\mathbf{E}_T(\mathbf{y}), \mathbf{E}'_T)_{\Gamma_{z^+}}, \end{aligned} \quad (30)$$

for (13), respectively. The parametrized discrete system reads

$$\mathbf{A}_{\text{dof}}(\mathbf{y}) \mathbf{c}_{\text{dof}}(\mathbf{y}) = \mathbf{P}^H \mathbf{A}(\mathbf{y}) \mathbf{P} \mathbf{c}_{\text{dof}}(\mathbf{y}) = \mathbf{P}^H \mathbf{f} = \mathbf{f}_{\text{dof}} \quad (31)$$

and the parameter-dependent scattering parameters are given as

$$S_{\alpha, mn}(\mathbf{y}) = \left(\mathbf{E}_T(\mathbf{y}) - \mathbf{E}_T^{\text{inc}}, \pi_T [\mathbf{E}_{\alpha, mn}] \right)_{\Gamma_{z^+}}, \quad \text{where } \alpha \in \{\text{TE}, \text{TM}\}. \quad (32)$$

3. Uncertainty Quantification

In this section, we consider the general problem of finding

$$\mathbf{u}(\mathbf{y}) \in \tilde{V} \text{ s.t. } \tilde{a}_{\mathbf{y}}(\mathbf{u}(\mathbf{y}), \mathbf{v}) = \tilde{l}_{\mathbf{y}}(\mathbf{v}) \quad \forall \mathbf{v} \in \tilde{V}, \quad (33)$$

where \tilde{V} denotes a suitable Hilbert space. It may represent the model of Section 2.2, or other parametrized differential equations with a continuous sesquilinear form $\tilde{a}_{\mathbf{y}}(\cdot, \cdot)$ and a continuous (anti)linear form $\tilde{l}_{\mathbf{y}}(\cdot)$. We assume the map

$\mathbf{u} : \Xi \rightarrow \tilde{V}$ to be well-defined and sufficiently smooth. We are interested in the model's response which may be the solution $\mathbf{u}(\mathbf{y})$ itself or a functional $J_{\mathbf{y}}(\mathbf{u}(\mathbf{y}))$, e.g. a scattering parameter, commonly referred to as the QoI. In this work, we focus on single-valued and complex QoIs, i.e. $J_{\mathbf{y}}(\mathbf{u}(\mathbf{y})) \in \mathbb{C}$. For brevity of notation and owing to the well-posedness of the system, we shall replace $J_{\mathbf{y}}(\mathbf{u}(\mathbf{y}))$ with $J(\mathbf{y})$, where J can be understood as an abstract representation of the map from the input parameters to the QoI.

We now assume that the input parameters are given as independent RVs Y_n , $n = 1, 2, \dots, N$. We introduce the random vector $\mathbf{Y} = (Y_1, Y_2, \dots, Y_N)$, defined on the probability space (Θ, Σ, P) , where Θ denotes the sample space, Σ the set of events and P the probability measure, its image set $\Xi = \Xi_1 \times \Xi_2 \cdots \times \Xi_N \subset \mathbb{R}^N$ and its probability density function (PDF) $\varrho(\mathbf{y}) = \prod_{n=1}^N \varrho_n(y_n)$, such that $\mathbf{Y} : \Theta \rightarrow \Xi$ and $\varrho : \Xi \rightarrow \mathbb{R}_+$. Then, the parameter vector represents a realization of the random vector, i.e. $\mathbf{y} = \mathbf{Y}(\theta) \in \Xi$, $\theta \in \Theta$.

In this case, the QoI is itself a RV. We are interested in quantifying uncertainty with respect to the QoI, e.g. by computing its statistical moments, PDF, quantiles, etc. In the case where the QoI is smooth (ideally, analytic) with respect to the input RVs, spectral UQ methods [32, 50] may be employed. Then, J may be approximated by polynomials such that

$$J(\mathbf{y}) \approx \tilde{J}(\mathbf{y}) = \sum_{m=0}^{M-1} s_m \Psi_m(\mathbf{y}), \quad (34)$$

where $\Psi_m : \Xi \rightarrow \mathbb{R}$ are multivariate polynomials and $s_m \in \mathbb{C}$ the associated polynomial coefficients. Once an approximation in the form of (34) is available, it can be used as an inexpensive substitute of the original computational model for sampling-based computations. Alternatively, some statistical information regarding the QoI can be derived directly from the coefficients. In the context of the present work, we will use approximations in the form of (34), based either on gPC [51, 52, 53, 54, 25] or on sparse grid interpolation [24, 55, 56, 40, 57, 42, 58, 46, 26].

3.1. Generalized polynomial chaos

As in [50, 25], we shall focus on gPC expansions based on global orthogonal polynomials. The correspondence between commonly used PDFs and families of orthogonal polynomials can be sought in the Wiener-Askey scheme [25]. We introduce the multi-index $\mathbf{p} = (p_1, p_2, \dots, p_N) \in \mathbb{N}_0^N$ holding the polynomial degree per parameter and the multivariate polynomials $\Psi_{\mathbf{p}}(\mathbf{y}) = \prod_{n=1}^N \psi_{p_n}(y_n)$. The orthogonality condition reads

$$\mathbb{E}[\Psi_{\mathbf{p}} \Psi_{\mathbf{q}}] = \int_{\Xi} \Psi_{\mathbf{p}}(\mathbf{y}) \Psi_{\mathbf{q}}(\mathbf{y}) \varrho(\mathbf{y}) \, d\mathbf{y} = \mathbb{E}[\Psi_{\mathbf{p}}^2] \delta_{\mathbf{p}, \mathbf{q}}, \quad (35)$$

where $\delta_{\mathbf{p}, \mathbf{q}} = \delta_{p_1, q_1} \delta_{p_2, q_2} \cdots \delta_{p_N, q_N}$. Typically, a total-degree polynomial basis is employed, such that $|\mathbf{p}| = p_1 + p_2 + \cdots + p_N \leq p_{\max} \in \mathbb{N}_0$. Equivalently, the total-degree polynomial basis consists of all polynomials $\{\Psi_{\mathbf{p}} : \mathbf{p} \in \Lambda_{p_{\max}}^{\text{TD}}\}$, where

$$\Lambda_{p_{\max}}^{\text{TD}} := \{\mathbf{p} : |\mathbf{p}| \leq p_{\max}\}, \quad (36)$$

is a multi-index set. Then, the number of approximation terms is $M = \frac{(N+p_{\max})!}{N! p_{\max}!}$ and the multivariate gPC approximation reads

$$J(\mathbf{y}) \approx \tilde{J}(\mathbf{y}) = \sum_{|\mathbf{p}| \leq p_{\max}} s_{\mathbf{p}} \Psi_{\mathbf{p}}(\mathbf{y}) = \sum_{\mathbf{p} \in \Lambda_{p_{\max}}^{\text{TD}}} s_{\mathbf{p}} \Psi_{\mathbf{p}}(\mathbf{y}). \quad (37)$$

In the present work, the series coefficients $s_{\mathbf{p}} \in \mathbb{C}$ are computed by means of pseudo-spectral projection [52, 53]. Readers interested in the alternative option of least-squares regression are referred to [51, 54]. We multiply (37) with $\Psi_{\mathbf{q}}$, where $|\mathbf{q}| \leq p_{\max}$. Then, we apply the expectation operator on both sides of the resulting equation. Under the orthogonality condition (35), the series coefficients $s_{\mathbf{p}}$ are given as

$$s_{\mathbf{p}} = \frac{\mathbb{E}[J \Psi_{\mathbf{p}}]}{\mathbb{E}[\Psi_{\mathbf{p}}^2]} = \frac{\int_{\Xi} J(\mathbf{y}) \Psi_{\mathbf{p}}(\mathbf{y}) \varrho(\mathbf{y}) \, d\mathbf{y}}{\int_{\Xi} \Psi_{\mathbf{p}}(\mathbf{y}) \Psi_{\mathbf{p}}(\mathbf{y}) \varrho(\mathbf{y}) \, d\mathbf{y}}. \quad (38)$$

In (38), the multivariate integrals of the numerator are typically computed by means of numerical integration [32], e.g. (Quasi-) Monte Carlo (MC) sampling or Gauss quadrature. For Wiener-Askey polynomials, the denominator can be determined analytically.

3.2. Sparse grid interpolation

Approximations based on sparse grid interpolation are commonly referred to as sparse grid stochastic collocation methods [24, 58, 26]. Those methods are based on combinations of univariate interpolation rules, defined by an interpolation level $\ell_n \in \mathbb{N}_0$, a monotonically increasing level-to-nodes function $m_n : \mathbb{N}_0 \rightarrow \mathbb{N}$, where $m_n(\ell_n) =: m_{\ell_n}$ and $m_n(0) = 1$ and a grid of m_{ℓ_n} interpolation nodes

$$Z_{\ell_n} = \left\{ y_n^{(i_n)} \right\}_{i_n=0}^{m_{\ell_n}-1}. \quad (39)$$

Introducing the multi-index $\boldsymbol{\ell} = (\ell_1, \ell_2, \dots, \ell_N) \in \mathbb{N}_0^N$, the tensor-product multivariate approximation is obtained as

$$J(\mathbf{y}) \approx \tilde{J}(\mathbf{y}) = \sum_{\mathbf{i}; \mathbf{y}^{(\mathbf{i})} \in Z_{\boldsymbol{\ell}}} J(\mathbf{y}^{(\mathbf{i})}) L_{\boldsymbol{\ell}, \mathbf{i}}(\mathbf{y}), \quad (40)$$

where $\mathbf{y}^{(\mathbf{i})} = (y_1^{(i_1)}, y_2^{(i_2)}, \dots, y_N^{(i_N)}) \in Z_{\boldsymbol{\ell}}$ are multivariate interpolation nodes, uniquely identified by the multi-index $\mathbf{i} = (i_1, i_2, \dots, i_N) \in \mathbb{N}_0^N$, $Z_{\boldsymbol{\ell}} = Z_{\ell_1} \times Z_{\ell_2} \times \dots \times Z_{\ell_N}$ is the tensor grid of interpolation nodes and $L_{\boldsymbol{\ell}, \mathbf{i}}$ are multivariate Lagrange polynomials, such that

$$L_{\boldsymbol{\ell}, \mathbf{i}}(\mathbf{y}) = \prod_{n=1}^N l_{\ell_n, i_n}(y_n), \quad \text{where } l_{\ell_n, i_n}(y_n) := \begin{cases} \prod_{k=1, k \neq i_n}^{m_{\ell_n}} \frac{y_n - y_n^{(k)}}{y_n^{(i_n)} - y_n^{(k)}}, & \ell_n \neq 0, \\ 1, & \ell_n = 0. \end{cases} \quad (41)$$

It should be noted that (41) is used for the ease of exposition, in the actual implementation the barycentric representation is used. Since $J(\mathbf{y})$ has to be evaluated for each $\mathbf{y}^{(\mathbf{i})} \in Z_{\boldsymbol{\ell}}$, the complexity of the tensor-product approach is $\mathcal{O}(m_k^N)$, where $m_k := \max_n m_{\ell_n}$.

This complexity can be mitigated to $\mathcal{O}(m_k (\log m_k)^{N-1})$ without compromising the approximation's accuracy by employing Smolyak sparse grids [59]. We introduce the approximation level $k \in \mathbb{N}_0$ and define the multi-index set Λ_k , such that

$$\Lambda_k := \{ \boldsymbol{\ell} : |\boldsymbol{\ell}| \leq k \}. \quad (42)$$

Then, the sparse grid of multivariate interpolation nodes Z_{Λ_k} is constructed as

$$Z_{\Lambda_k} = \bigcup_{k-N+1 \leq |\boldsymbol{\ell}| \leq k} Z_{\boldsymbol{\ell}}, \quad (43)$$

and the interpolation is given by

$$\mathcal{I}_{\Lambda_k}[J](\mathbf{y}) = \sum_{\mathbf{i}; \mathbf{y}^{(\mathbf{i})} \in Z_{\Lambda_k}} J(\mathbf{y}^{(\mathbf{i})}) L_{\boldsymbol{\ell}, \mathbf{i}}(\mathbf{y}). \quad (44)$$

3.2.1. Leja nodes, hierarchical interpolation and adaptivity

As shown in [55], Smolyak formulas are in general not interpolatory, unless based on nested sequences of univariate interpolation nodes, such that $Z_{\ell_{n-1}} \subset Z_{\ell_n}$. Moreover, to ensure accuracy and fast convergence of the approximation, the interpolation nodes should be chosen in agreement with the PDFs $\varrho_n(y_n)$.

In the context of the present work, we opt for weighted Leja interpolation nodes, as in [42]. Given a univariate, continuous and positive weight function, here given by a univariate PDF $\varrho_n(y_n)$, $\varrho_n : \Xi_n \rightarrow \mathbb{R}_+$, a sequence of univariate Leja nodes $y_n^{(k)} \in \Xi_n$, $k = 0, 1, 2, \dots$, can be constructed by solving the optimization problem

$$y_n^{(K)} = \arg \min_{y_n \in \Xi_n} \sqrt{\varrho_n(y_n)} \prod_{k=0}^{K-1} |y_n - y_n^{(k)}|, \quad (45)$$

where the starting node $y_n^{(0)}$ is arbitrarily chosen. For further details on the construction of weighted Leja nodes and an analysis of their properties, see [42]. We justify the choice of Leja nodes as follows. First of all, Leja nodes satisfy the nestedness by construction. Secondly, they allow complete freedom in the choice of the level-to-nodes function $m_n(\ell_n)$. Finally, they can be tailored to any given PDF. In comparison, the commonly employed Clenshaw-Curtis nodes would restrict us to uniform distributions and to the rapidly growing level-to-nodes function $m_n(\ell_n) = 2^{\ell_n} + 1$.

Data: QoI $J(\mathbf{y})$, multi-index set Λ , tolerance ϵ , budget B

Result: sparse grid $Z_{\Lambda \cup \Lambda_+^{\text{adm}}}$, approximation $\mathcal{I}_{\Lambda \cup \Lambda_+^{\text{adm}}}[J]$

repeat

- Compute the admissible set Λ_+^{adm} , as in (52).
- Compute the hierarchical surpluses $s_\ell, \forall \ell \in \Lambda_+^{\text{adm}}$, as in (50).
- Find the multi-index $\ell \in \Lambda_+^{\text{adm}}$ with the maximum error indicator $|s_\ell|$.
- Compute the approximation $\mathcal{I}_{\Lambda \cup \ell}$, as in (49).
- Set $\Lambda = \Lambda \cup \ell$.

until stopping criterion (53) fulfilled;

Algorithm 1: Dimension-adaptive interpolation.

In the following, we employ the level-to-nodes function $m_n(\ell_n) = \ell_n + 1, \ell_n \in \mathbb{N}_0$, and denote with $y_n^{(\ell_n)}$ the single extra node corresponding to interpolation level ℓ_n , i.e. $y_n^{(\ell_n)} = Z_{\ell_n} \setminus Z_{\ell_n-1}$.

In the multivariate case, nested grids of multivariate interpolation nodes can be constructed by enforcing the use of downward-closed (also, monotone or lower) multi-index sets [40, 60]. Such sets are known to preserve the telescopic properties of the series in (44) [60]. Moreover, sequences of nested, downward-closed multi-index sets result in polynomial approximations of increasing accuracy [40]. Given a multi-index set Λ , let us first define its forward and backward neighbor multi-index sets, Λ_+ and Λ_- , respectively, such that

$$\Lambda_+ := \{\ell + \mathbf{e}_n, \forall \ell \in \Lambda, \forall n = 1, 2, \dots, N\}, \quad (46)$$

$$\Lambda_- := \{\ell - \mathbf{e}_n, \forall \ell \in \Lambda, \forall n = 1, 2, \dots, N : \ell_n > 0\}, \quad (47)$$

where \mathbf{e}_n is the n -th unit vector. Then, Λ is said to be downward-closed if and only if

$$\Lambda_- \subset \Lambda. \quad (48)$$

Assuming now a multi-index $\ell \notin \Lambda$ such that $\Lambda \cup \ell$ is downward-closed, it holds that $Z_\Lambda \subset Z_{\Lambda \cup \ell}$ and $\mathbf{y}^{(\ell)} = Z_{\Lambda \cup \ell} \setminus Z_\Lambda$. Then, (44) can be naturally transformed into the hierarchical interpolation

$$\mathcal{I}_{\Lambda \cup \ell}[J](\mathbf{y}) = \mathcal{I}_\Lambda[J](\mathbf{y}) + s_\ell H_\ell(\mathbf{y}^{(\ell)}), \quad (49)$$

where the coefficients $s_\ell \in \mathbb{C}$, known as ‘‘hierarchical surpluses’’, are given by

$$s_\ell = J(\mathbf{y}^{(\ell)}) - \mathcal{I}_\Lambda[J](\mathbf{y}^{(\ell)}), \quad (50)$$

and H_ℓ are multivariate hierarchical polynomials, defined as

$$H_\ell(\mathbf{y}) = \prod_{n=1}^N h_{\ell_n}(y_n), \quad \text{where} \quad h_{\ell_n}(y_n) := \begin{cases} \prod_{k=0}^{\ell_n-1} \frac{y_n - y_n^{(k)}}{y_n^{(\ell_n)} - y_n^{(k)}}, & \ell_n \neq 0, \\ 1, & \ell_n = 0. \end{cases} \quad (51)$$

The use of hierarchical polynomials has the advantage that the basis polynomials do not change as new nodes are added. Moreover, the hierarchical surpluses s_ℓ can be interpreted as error indicators, quantifying the contribution of interpolation node $\mathbf{y}^{(\ell)}$ to the already available approximation. This interpretation motivates the adaptive construction of the sparse grid approximation based on a posteriori error estimates. We consider a dimension-adaptive scheme, similar to the ones employed in [40, 60, 57, 42, 46], with minor modifications to address the case of complex QoIs. The scheme is presented in Algorithm 1. A detailed description follows.

Given a downward-closed multi-index set Λ , as well as the corresponding approximation $\mathcal{I}_\Lambda[J]$ and grid Z_Λ , we define the set of admissible neighbors Λ_+^{adm} , such that

$$\Lambda_+^{\text{adm}} := \{\ell \in \Lambda_+ : \ell \notin \Lambda \quad \text{and} \quad \{\ell\}_- \subset \Lambda\}. \quad (52)$$

Expanding Λ with admissible multi-indices $\ell \in \Lambda_+^{\text{adm}}$ guarantees that (48) is satisfied, and we thus construct a sequence of nested downward-closed sets [40]. In this work, the error indicator corresponding to each multi-index $\ell \in \Lambda_+^{\text{adm}}$ is chosen to be the modulus $|s_\ell|$ of the corresponding complex hierarchical surplus, however, other choices are possible, e.g. $\max(|\text{Re}\{s_\ell\}|, |\text{Im}\{s_\ell\}|)$. We update Λ with the multi-index $\ell \in \Lambda_+^{\text{adm}}$ corresponding to the maximum error indicator

$|s_\ell|$. The grid of interpolation nodes Z_Λ and the approximation \mathcal{I}_Λ are updated accordingly. This procedure is continued iteratively, until a budget of model evaluations B is reached. This criterion can be formulated as

$$\#Z_{\Lambda \cup \Lambda_+^{\text{adm}}} \geq B, \quad (53)$$

where $\#$ denotes the cardinality of a set. If an approximation is not readily available, the algorithm is initiated with $\Lambda = \{(0, 0, \dots, 0)\}$. After the termination of the algorithm, the approximation is constructed using the set $\Lambda \cup \Lambda_+^{\text{adm}}$.

3.3. Adjoint error estimation and adaptivity

We significantly improve Algorithm 1 by proposing the use of an adjoint error indicator to steer adaptivity. Adjoint error estimation is well established in the context of the FEM, see [61] and the references therein. It has been considered in a stochastic/parametric context [43, 44, 62], as well as for Clenshaw-Curtis adaptivity [45, 46]. Due to the exponential growth of Clenshaw-Curtis nodes, adjoint error estimation can result in a significant reduction of computational cost. In this work, we demonstrate that adjoint techniques can be beneficial for Leja adaptivity, too.

In this section we assume that $J(\mathbf{y}) = J_{\mathbf{y}}(\mathbf{u}(\mathbf{y}))$, $J_{\mathbf{y}} : V \rightarrow \mathbb{C}$, is a linear functional with respect to $\mathbf{u}(\mathbf{y})$. Generalizations to non-linear functionals are possible where techniques as in [63, Chapter 3.2] need to be applied. We rewrite the primal problem (33) as an operator equation: $\forall \mathbf{y} \in \Xi$, find $\mathbf{u}(\mathbf{y}) \in V$, such that

$$(L_{\mathbf{y}}\mathbf{u}(\mathbf{y}), \mathbf{v})_D = a_{\mathbf{y}}(\mathbf{u}(\mathbf{y}), \mathbf{v}) = l_{\mathbf{y}}(\mathbf{v}) \quad \forall \mathbf{v} \in V, \quad (54)$$

where $L_{\mathbf{y}} : V \rightarrow V$ denotes the primal operator. The dual problem is given as: $\forall \mathbf{y} \in \Xi$, find $\mathbf{z}(\mathbf{y}) \in V$, such that

$$(\mathbf{w}, L_{\mathbf{y}}^*\mathbf{z}(\mathbf{y}))_D = a_{\mathbf{y}}(\mathbf{w}, \mathbf{z}(\mathbf{y})) = J_{\mathbf{y}}(\mathbf{w}) \quad \forall \mathbf{w} \in V, \quad (55)$$

where $L_{\mathbf{y}}^* : V \rightarrow V$ denotes the adjoint operator defined by

$$(L_{\mathbf{y}}\mathbf{u}, \mathbf{v})_D = (\mathbf{u}, L_{\mathbf{y}}^*\mathbf{v})_D \quad \forall \mathbf{u}, \mathbf{v} \in V, \quad \forall \mathbf{y} \in \Xi. \quad (56)$$

The so-called primal-dual equivalence

$$J_{\mathbf{y}}(\mathbf{u}(\mathbf{y})) = (\mathbf{u}(\mathbf{y}), L_{\mathbf{y}}^*\mathbf{z}(\mathbf{y}))_D = (L_{\mathbf{y}}\mathbf{u}(\mathbf{y}), \mathbf{z}(\mathbf{y}))_D = l_{\mathbf{y}}(\mathbf{z}(\mathbf{y})) \quad (57)$$

follows directly from these definitions. Given polynomial approximations $\tilde{\mathbf{u}}, \tilde{\mathbf{z}}$ of the mappings $\mathbf{u}, \mathbf{z} : \Xi \rightarrow V$, we are interested in the error

$$\epsilon(\mathbf{y}) = J_{\mathbf{y}}(\mathbf{u}(\mathbf{y})) - \tilde{\mathbf{u}}(\mathbf{y}) = a_{\mathbf{y}}(\mathbf{u}(\mathbf{y}) - \tilde{\mathbf{u}}(\mathbf{y}), \mathbf{z}(\mathbf{y})) = l_{\mathbf{y}}(\mathbf{z}(\mathbf{y})) - a_{\mathbf{y}}(\tilde{\mathbf{u}}(\mathbf{y}), \mathbf{z}(\mathbf{y})). \quad (58)$$

Even if $\tilde{\mathbf{u}}, \tilde{\mathbf{z}}$ are replaced by their finite element counterparts, the error according to (58) is not readily computable, as it would require the computation of the adjoint \mathbf{z} for all $\mathbf{y} \in \Xi$. Following [43, 44], we propose to use the error indicator

$$\tilde{\epsilon}(\mathbf{y}) = a_{\mathbf{y}}(\mathbf{u}(\mathbf{y}) - \tilde{\mathbf{u}}(\mathbf{y}), \tilde{\mathbf{z}}(\mathbf{y})) = l_{\mathbf{y}}(\tilde{\mathbf{z}}(\mathbf{y})) - a_{\mathbf{y}}(\tilde{\mathbf{u}}(\mathbf{y}), \tilde{\mathbf{z}}(\mathbf{y})). \quad (59)$$

By exploiting the continuity of the sesquilinearform $a_{\mathbf{y}}(\cdot, \cdot)$, it can easily be shown that the error indicator (59) converges faster than the polynomial approximations $\tilde{\mathbf{u}}, \tilde{\mathbf{z}}$

$$|\epsilon(\mathbf{y}) - \tilde{\epsilon}(\mathbf{y})| = |a_{\mathbf{y}}(\mathbf{u}(\mathbf{y}) - \tilde{\mathbf{u}}(\mathbf{y}), \mathbf{z}(\mathbf{y})) - a_{\mathbf{y}}(\mathbf{u}(\mathbf{y}) - \tilde{\mathbf{u}}(\mathbf{y}), \tilde{\mathbf{z}}(\mathbf{y}))| \quad (60)$$

$$= |a_{\mathbf{y}}(\mathbf{u}(\mathbf{y}) - \tilde{\mathbf{u}}(\mathbf{y}), \mathbf{z}(\mathbf{y}) - \tilde{\mathbf{z}}(\mathbf{y}))| \quad (61)$$

$$\leq C\|\mathbf{u}(\mathbf{y}) - \tilde{\mathbf{u}}(\mathbf{y})\|_V\|\mathbf{z}(\mathbf{y}) - \tilde{\mathbf{z}}(\mathbf{y})\|_V. \quad (62)$$

We proceed by discussing the necessary adaptations to Algorithm 1, in order to incorporate the adjoint error indicator (59). Additionally to the polynomial approximation (49) of the single-valued and complex QoI, one needs to create polynomial approximations $\tilde{\mathbf{u}}(\mathbf{y}), \tilde{\mathbf{z}}(\mathbf{y})$ of the vector-valued primal and dual solution. Those can be obtained by using vector coefficients $\mathbf{u}_\ell, \mathbf{z}_\ell \in \mathbb{C}^{N_{\text{DoF}}}$ instead of the single-valued coefficients $s_\ell \in \mathbb{C}$ in (49). The polynomial approximations are constructed with the same multi-index set Λ as for the QoI, using the same polynomials $H_\ell(\mathbf{y})$.

Following [45], we carry out the following algorithmic modifications in the dimension-adaptive scheme. While Algorithm 1 uses the error indicators $|s_\ell|$, $\forall \ell \in \Lambda_+^{\text{adm}}$ by solving the respective linear system, we suggest the use of the adjoint-based error indicators $|\tilde{s}_\ell|$, where $\tilde{s}_\ell = \tilde{\epsilon}(\mathbf{y}^{(\ell)})$. As before, we choose the multi-index with the maximum error

Data: $\mathbf{A}_{\text{dof}}(\mathbf{y}), \mathbf{f}_{\text{dof}}(\mathbf{y}), \mathbf{J}_{\text{dof}}(\mathbf{y}), \Lambda, \epsilon, B$

Result: sparse grid $Z_{\Lambda \cup \Lambda_+^{\text{adm}}}$, approximation $\mathcal{I}_{\Lambda \cup \Lambda_+^{\text{adm}}}[J]$

repeat

 Compute the admissible set Λ_+^{adm} , as in (52).

 Compute the error indicators $|\tilde{s}_\ell|$, where $\tilde{s}_\ell = \tilde{\epsilon}(\mathbf{y}^{(\ell)})$, $\forall \ell \in \Lambda_+^{\text{adm}}$.

 Find the multi-index $\ell \in \Lambda_+^{\text{adm}}$ with the maximum error indicator.

 Compute the hierarchical surpluses $s_\ell, \mathbf{u}_\ell, \mathbf{z}_\ell$ as in (50), by solving the linear systems for primal and dual solution.

 Compute the approximation $\mathcal{I}_{\Lambda \cup \ell}$, as in (49), and the corresponding approximations of primal and dual solution.

 Set $\Lambda = \Lambda \cup \ell$.

until *stopping criterion fulfilled*;

Algorithm 2: Adjoint error-based, dimension-adaptive interpolation.

indicator, solve the corresponding linear system and update the polynomial approximations of the primal and the dual solution, as well as of the QoI. This scheme is summarized in Algorithm 2. After the termination of the algorithm, the approximation can be constructed with the set $\Lambda \cup \Lambda_+^{\text{adm}}$, such that the already computed adjoint-based error indicators are used as the hierarchical surpluses corresponding to the admissible neighbors, i.e. $s_\ell = \tilde{s}_\ell$, $\forall \ell \in \Lambda_+^{\text{adm}}$. The error indicator (59) can be further exploited in order to improve the polynomial surrogate model of the QoI. In particular, one can replace the single-valued QoI $J(\mathbf{y})$ by

$$\tilde{J}(\mathbf{y}) = \mathcal{I}_\Lambda[J](\mathbf{y}) + \tilde{\epsilon}(\mathbf{y}), \quad (63)$$

such that the computed polynomial approximation is corrected by the adjoint-error indicator, before continuing with further approximation refinements using Algorithm 1. We emphasize that no further linear equation system has to be solved in order to evaluate (63).

Remark 3.1. Relating the methodology of this section to the scattering in periodic media, the linear functional is given by

$$S_{\alpha, mn}(\mathbf{y}) = \underbrace{(\mathbf{E}_T(\mathbf{y}), \pi_T[\mathbf{E}_{\alpha, mn}])_{\Gamma_{z^+}}}_{=J(\mathbf{E})} - (\mathbf{E}_T^{\text{inc}}, \pi_T[\mathbf{E}_{\alpha, mn}])_{\Gamma_{z^+}}, \quad \text{where } \alpha \in \{\text{TE}, \text{TM}\}. \quad (64)$$

The strong formulation of the adjoint problem (55) reads

$$\nabla \times \left(\frac{1}{\mu_r^*} \nabla \times \mathbf{z} \right) - \omega^2 \mu_0 \epsilon^* \mathbf{z} = 0 \quad \text{in } \Omega, \quad (65a)$$

$$\mathbf{z}_T|_{\Gamma_{x^+}} = \mathbf{z}_T|_{\Gamma_{x^-}} e^{j\psi_x} \quad \text{on } \Gamma_{x^+} \cup \Gamma_{x^-}, \quad (65b)$$

$$\mathbf{z}_T|_{\Gamma_{y^+}} = \mathbf{z}_T|_{\Gamma_{y^-}} e^{j\psi_y} \quad \text{on } \Gamma_{y^+} \cup \Gamma_{y^-}, \quad (65c)$$

$$\mathbf{z}_t = 0 \quad \text{on } \Gamma_{z^-}, \quad (65d)$$

$$\mathbf{e}_z \times \left(\frac{j}{\omega \mu_0} \nabla \times \mathbf{z} \right) - \sum_{\alpha, mn} \tilde{d}_{\alpha, mn}^* Y_{\alpha, mn}^* \pi_T[\mathbf{E}_{\alpha, mn}] = -\frac{j}{\omega \mu_0} \pi_T[\mathbf{E}_{\alpha, mn}] \quad \text{on } \Gamma_{z^+}, \quad (65e)$$

where $\tilde{d}_{\alpha, mn} = (\pi_T[\mathbf{E}_{\alpha, mn}], \mathbf{z}_T)_{\Gamma_{z^+}}$. If first order Floquet boundary conditions (13) are used for the primal problem, the respective boundary condition of the dual problem becomes

$$\mathbf{e}_z \times \left(\frac{j}{\omega \mu_0} \nabla \times \mathbf{z} \right) + \frac{\mathbf{k}_t^{\text{inc}}}{\omega \mu_0 k_z^{\text{inc}}} (\mathbf{k}_t^{\text{inc}} \cdot \mathbf{z}_T) + \frac{k_z^{\text{inc}}}{\omega \mu_0} \mathbf{z}_T = -\frac{j}{\omega \mu_0} \pi_T[\mathbf{E}_{\alpha, mn}] \quad \text{on } \Gamma_{z^+}. \quad (66)$$

Discretization of the adjoint problem (55) yields the discrete matrix equation

$$\mathbf{A}_{\text{dof}}^H \mathbf{z}_{\text{dof}} = \mathbf{P}^H \mathbf{J} = \mathbf{J}_{\text{dof}}, \quad \text{where } \mathbf{J} \in \mathbb{C}^{N_h}. \quad (67)$$

and the discrete version of the error indicator (59) reads

$$\tilde{\epsilon}_h(\mathbf{y}) = \tilde{\mathbf{z}}_{\text{dof}}^H(\mathbf{y}) \mathbf{f}_{\text{dof}}(\mathbf{y}) - \tilde{\mathbf{z}}_{\text{dof}}^H(\mathbf{y}) \mathbf{A}_{\text{dof}}(\mathbf{y}) \tilde{\mathbf{c}}_{\text{dof}}(\mathbf{y}). \quad (68)$$

Note that the dual solution can be obtained with negligible cost in many cases, e.g. if the primal problem is solved with a sparse LU decomposition $\mathbf{A}_{\text{dof}} = \mathbf{L}\mathbf{U}$, for the respective dual problem we obtain $\mathbf{A}_{\text{dof}}^H = (\mathbf{L}\mathbf{U})^H = \mathbf{U}^H \mathbf{L}^H$.

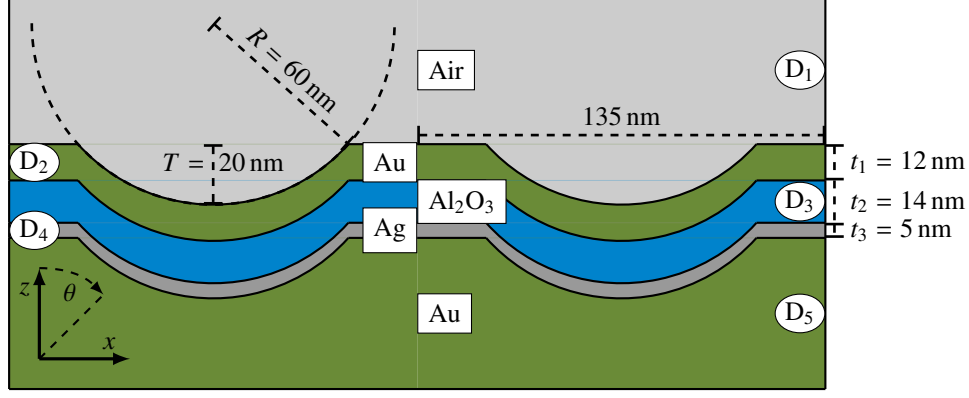


Figure 3: Design of considered optical grating coupler.

4. Application

We apply the UQ methods presented in Section 3 to an optical grating coupler model [5], [64]. First, we describe the parametrized numerical model. Then, we quantify the impact of geometric and material uncertainties for the case of single-frequency excitation. We consider both the dimension-adaptive collocation method with Leja nodes and a gPC approximation, where discrete projection is used to determine the coefficients. gPC is used here mainly for comparison. Additionally, the decay of the gPC coefficients gives insight into the regularity of the input-to-output mapping, justifying the use of spectral methods numerically. Finally, we consider the case of a variable frequency and discuss the necessary adaptations for performing UQ for resonances. Both the deterministic numerical model and the UQ studies rely on open-source software.

For general periodic structures, we must distinguish between two types of uncertainties. In this work we focus on *global* uncertainties, i.e. we assume that all unit cells are identically affected, modeling a systematic offset in the fabrication process. We do not address *local* uncertainties leading to a violation of the periodicity and different unit cells.

4.1. Numerical model

The considered grating coupler [5] couples power from an incident TM polarized plane wave, such that

$$\pi_T [\mathbf{E}^{\text{inc}}] = \pi_T [\mathbf{E}_{\text{TM},00}], \quad \text{at } \Gamma_{z^+},$$

with propagation direction $\theta^{\text{inc}} = 53^\circ$, $\phi^{\text{inc}} = 0^\circ$, directly into a MIM plasmon mode.

The structure's design, shown in Fig. 3, is assumed to be periodic in the x direction and infinitely extended in the y direction. The reflection coefficients (26a), (26b) at the upper boundary Γ_{z^+} correspond to the coupling efficiency of the structure, such that larger reflection coefficients indicate a lower coupling efficiency. Therefore, the scattering parameter $S := S_{\text{TM},00}$ is considered as the QoI in the following. Note that we focus on the fundamental reflection coefficient $S_{\text{TM},00}$ because, for this particular model, all other scattering parameters have negligible amplitudes.

We model the material properties based on measurement data for noble metals provided by Johnson and Christy in [65] and presented in Table 1. We focus on the frequency range $f_{\text{min}} = 400$ THz to $f_{\text{max}} = 430$ THz, see Fig. 4. The data is experimentally determined by reflectivity studies and is therefore given in terms of the refractive indices n and the extinction coefficients κ for gold and silver, respectively. From those, one obtains the complex permittivity as in [2, Chapter 1.1], i.e.

$$\epsilon = (n^2 - \kappa^2 - j(2n\kappa)) \epsilon_0. \quad (69)$$

The data is provided for discrete frequency sample points. Therefore, we need to interpolate in between those sample points in order to obtain the dispersive behaviour of the permittivity $\epsilon(\omega)$. Since we only focus on a rather small

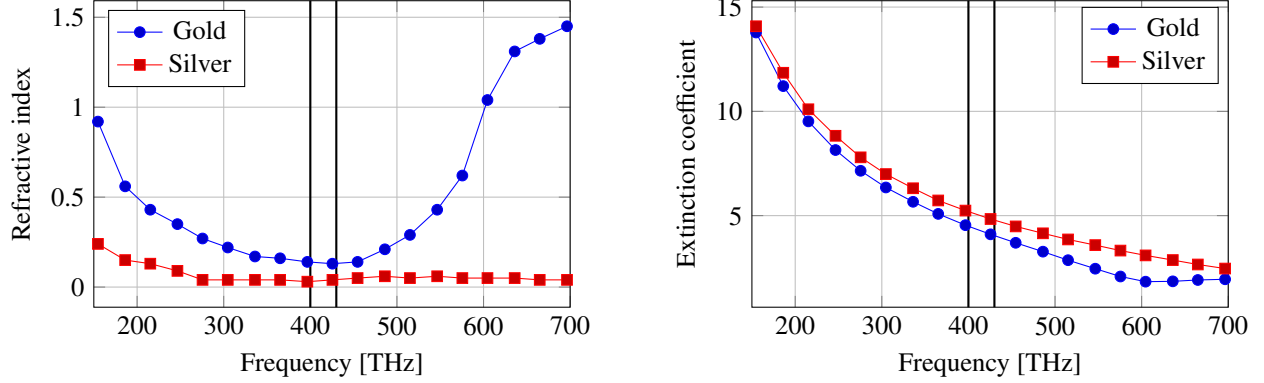


Figure 4: Dispersive optical constants of gold and silver [65]. The black vertical lines define the considered frequency range.

Index i	Energy [eV]	Frequency f_i [THz]	Refractive index n_i^{Au}	Extinction coefficient κ_i^{Au}	Refractive index n_i^{Ag}	Extinction coefficient κ_i^{Ag}
0	1.64	396.55	0.14 ± 0.02	4.542 ± 0.015	0.03 ± 0.02	5.242 ± 0.015
1	1.76	425.57	0.13 ± 0.02	4.103 ± 0.010	0.04 ± 0.02	4.838 ± 0.010
2	1.88	454.58	0.14 ± 0.02	3.697 ± 0.007	0.05 ± 0.02	4.483 ± 0.007

Table 1: Material data, taken from [65].

frequency range, we apply polynomial interpolation

$$n^{\text{Au}}(\omega) = \sum_{i=0}^2 n_i^{\text{Au}} l_i(\omega), \quad n^{\text{Ag}}(\omega) = \sum_{i=0}^2 n_i^{\text{Ag}} l_i(\omega), \quad (70)$$

$$\kappa^{\text{Au}}(\omega) = \sum_{i=0}^2 \kappa_i^{\text{Au}} l_i(\omega), \quad \kappa^{\text{Ag}}(\omega) = \sum_{i=0}^2 \kappa_i^{\text{Ag}} l_i(\omega), \quad (71)$$

where

$$l_i(\omega) = \prod_{j=0, j \neq i}^2 \frac{\omega - \omega_j}{\omega_i - \omega_j}, \quad \omega_i = 2\pi f_i,$$

are 2nd order Lagrange polynomials and $f_i, n_i^{\text{Au}}, \kappa_i^{\text{Au}}, n_i^{\text{Ag}}, \kappa_i^{\text{Ag}}, i = 0, 1, 2$ are given.

We proceed with the implementation of the deterministic numerical model, as well as its parametrization. The periodic mesh for the nominal design, needed for imposing the quasi-periodic boundary conditions (4a), (4b), is created using GMSH [66]. Since for this particular structure only the fundamental Floquet modes propagate and all higher order modes are attenuated to a negligible amplitude at Γ_{z^+} , we can use the first order Floquet boundary condition (13), leading to the sesquilinear form (23). We use FENICS [67] as FE library to assemble the FE matrix \mathbf{A} and right-hand side (RHS) \mathbf{f} (see (25)), as well as the linear functional \mathbf{J}_{dof} used for the numerical approximation of the scattering parameter

$$S_{\text{TM},00} = \left(\mathbf{E}_{\text{T}} - \mathbf{E}_{\text{T}}^{\text{inc}}, \pi_{\text{T}} [\mathbf{E}_{\text{TM},00}] \right)_{\Gamma_{z^+}} \approx \mathbf{J}_{\text{dof}}^{\text{T}} \mathbf{c}_{\text{dof}} - 1.$$

Since FENICS is not able to deal with complex numbers, we assemble the real and the imaginary parts of the matrix and the vectors separately. We then use NUMPY and SCIPY to impose the quasi-periodic boundary conditions (4a), (4b) and solve the resulting linear system (25) by a sparse LU decomposition, respectively. Using 2nd order Nédélec elements of the 1st kind, we end up with 56 200 DoFs and achieve an accuracy of $\approx 10^{-3}$ in the scattering parameter. The reference solutions for different frequency sample points are computed with a commercial software [68] employing an adaptively refined mesh of higher order curved elements. Since a sparse LU decomposition is used to solve the resulting linear system, the adjoint solution \mathbf{z}_{dof} is obtained with negligible costs.

To incorporate changes in the geometry parameters without the need to re-mesh, a design element approach is applied [69]: First, an initial mesh is created using GMSH for the initial geometry parameters $\mathbf{y}^{\text{nominal}}$. We describe

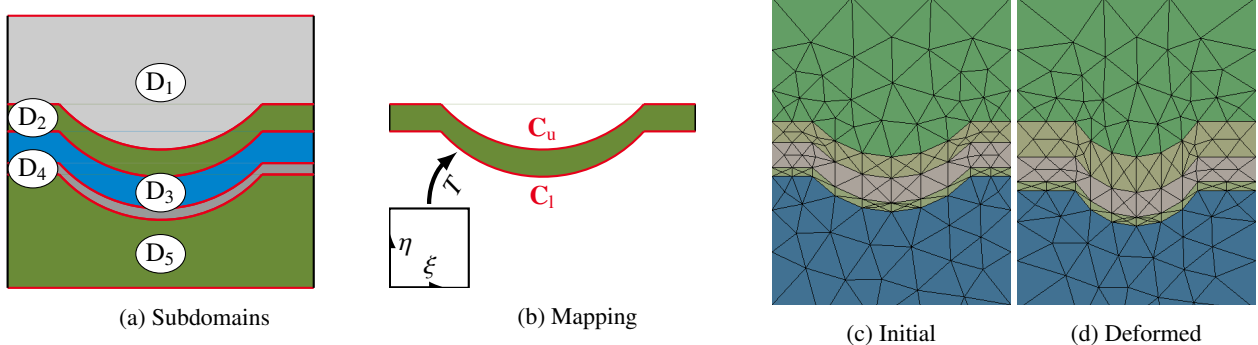


Figure 5: a) design elements. b) mapping from unit square. c) initial mesh (coarse for illustration) for nominal design $\mathbf{y}^{\text{nominal}}$. d) deformed mesh for $R = 40$ nm, $t_1 = 20$ nm.

Parameter	Nominal value	Variation
Grating radius R	60 nm	± 0.5 nm
Gold layer thickness t_1	12 nm	± 0.5 nm
Alumina layer thickness t_2	14 nm	± 0.5 nm
Silver layer thickness t_3	5 nm	± 0.5 nm
Grating depth T	20 nm	± 0.5 nm

Table 2: Uncertain geometrical parameters.

all (material) interfaces, illustrated in Fig. 5 in red color, using non-uniform rational B-splines (NURBS) [70]. Each NURBS curve

$$\mathbf{C}_i(\xi; \mathbf{y}) = \sum_{j=0}^n R_j(\xi) \mathbf{P}_{j,i}(\mathbf{y}), \quad \xi \in [0, 1] \quad (72)$$

is a superposition of rational basis functions $R_j(\xi)$ weighted by control points \mathbf{P}_j . We then define mappings

$$\mathbf{T}_m(\xi, \eta; \mathbf{y}) = \eta \mathbf{C}_{m,u}(\xi; \mathbf{y}) + (1 - \eta) \mathbf{C}_{m,l}(\xi; \mathbf{y}), \quad m = 1, \dots, M, \quad (73)$$

from the unit square $[0 \leq \xi \leq 1] \times [0 \leq \eta \leq 1]$ to each design element $D_i(\mathbf{y})$ (see Fig. 5). Thereby, the subscripts u and l refer to the upper and lower NURBS curve of the design element, respectively. Given the initial mesh, for each mesh node j with coordinates \mathbf{x}_j inside the design element D_m , the respective coordinates ξ_j, η_j on the unit square are found by solving the non-linear root finding problem

$$\text{find } \xi_j, \eta_j \in [0, 1], \text{ s.t. } \mathbf{T}_m(\xi_j, \eta_j; \mathbf{y}^{\text{nominal}}) - \mathbf{x}_j = \mathbf{0}, \quad \mathbf{x}_j \in D_m(\mathbf{y}^{\text{nominal}}). \quad (74)$$

Problem (74) can be reformulated as an optimization problem and is solved here using sequential quadratic programming (SQP) [71, Chapter 18]. In order to ensure convergence of SQP, one might need to choose adequate initial values, which depend on the chosen parametrization of the NURBS curves. Given the coordinates ξ_j, η_j for each mesh node j , we can deform the mesh by moving the mesh nodes to the new coordinates obtained by evaluating the mapping (73) for different geometry parameters \mathbf{y} .

4.2. Single frequency calculations

In this subsection, we consider a fixed frequency $\omega = 2\pi(414 \text{ THz})$ and $N = 17$ random input parameters \mathbf{Y} , in particular 5 geometrical parameters presented in Table 2 and the 12 material parameters given in Table 1. As introduced in Sec. 2, both the uncertain geometry and the uncertain material coefficients are modeled by an uncertain complex permittivity $\epsilon(\mathbf{x}, \mathbf{y})$, see (27).

We assume that the RVs Y_n , $n = 1, 2, \dots, N = 17$, are independent, uncorrelated and distributed in the ranges defined by their nominal values and variations. The variations of the material parameters are chosen according to the

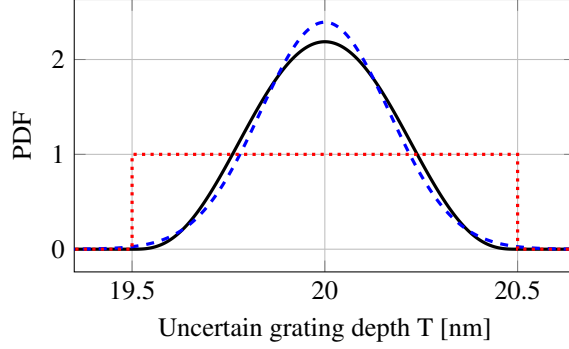


Figure 6: Black: PDF of beta distributed grating depth with support in [19.5 nm, 20.5 nm]. Blue, dashed: PDF of normal distribution with $\mu = 20$ nm and $\sigma = \frac{0.5}{3}$ nm. Red, dotted: PDF of uniform distribution with support in [19.5 nm, 20.5 nm].

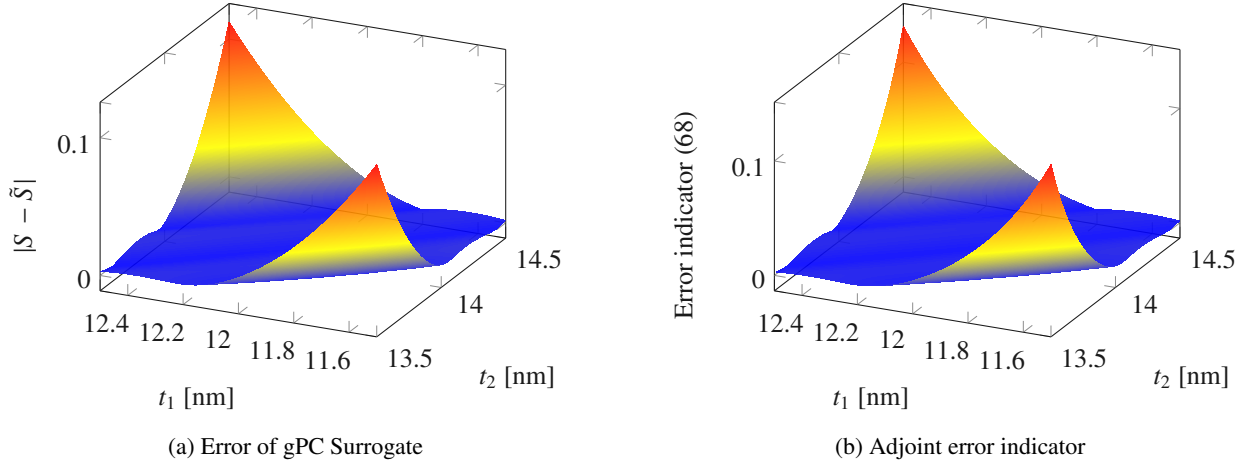


Figure 7: Adjoint-error indicator (68) for a two dimensional parameter space.

error estimate provided by Johnson and Christy *based on the instrumental accuracy of the reflection and transmission measurements* [65] while only small variations of the geometrical parameters in the range of ± 0.5 nm are considered.

Assuming uniformly distributed RVs would keep the parameter realizations bounded in the desired ranges, however, this would be a very restrictive assumption. Normal RVs would be a more realistic choice, which could, however, lead to unphysical parameter realizations, e.g. negative geometry values, due to their unbounded support. In this work, we opt for beta distributions, which have bounded support and can approximate normal distributions for suitable choices of their shape parameters [50, Appendix B]. The shape parameters are chosen based on the results of a series of Kolmogorov-Smirnov fitting tests [72]. Fig. 6 presents such an approximation for the grating depth parameter. The corresponding PDF for each RV $\{Y_n\}_{n=1}^N$ reads

$$\varrho(y_n, l_n, c_n) = \frac{140}{(u_n - l_n)^7} \begin{cases} (y_n - l_n)^3 (u_n - y_n)^3 & l_n < y_n < u_n, \\ 0 & \text{else,} \end{cases} \quad (75)$$

where l_n and u_n denote the lower and upper bound, respectively.

To illustrate the accuracy of the adjoint error indicator presented in Sec. 3.3, we first consider only two uncertain parameters, i.e. the thickness of the upper gold layer t_1 and the thickness of the dielectric layer t_2 . We use CHAOSPY [73] to build a 2nd order gPC approximation of the scattering parameter S , the primal solution \mathbf{E} , and the dual solution \mathbf{z} . The coefficients are obtained by pseudo-spectral projection (38) using a 3rd order Gauss quadrature. In Fig. 7 the error of the approximation $|S(t_1, t_2) - \tilde{S}(t_1, t_2)|$ and the corresponding adjoint error estimate (68) are shown. It is noticeable that the adjoint representation captures the error very well.

Next, we consider all 17 uncertain parameters given in Table 1 and Table 2. We construct gPC and Leja adaptive approximations, using both Algorithm 1 and the adjoint-based Algorithm 2 for the latter. CHAOSPY is used for the gPC

	#LU	#FB	#Res	Max. Error (77)	Mean Error (76)
Total-degree gPC	613	613	0	2.30×10^{-1}	6.23×10^{-3}
Adaptive Leja (without adjoints)	613	613	0	1.73×10^{-2}	2.07×10^{-4}
Adaptive Leja (with adjoints)	421	842	613	1.73×10^{-2}	2.07×10^{-4}
Adaptive Leja (without adjoints)	12000	12000	0	1.23×10^{-3}	5.21×10^{-6}
Adaptive Leja (with adjoints)	421	842	12000	1.01×10^{-3}	5.17×10^{-6}

Table 3: Accuracy and computational cost of different polynomial approximations for 17 input RVs. #LU refers to the dominating costs for the assembly and sparse LU decomposition of the system matrices. #FB and #Res denote the number of forward-backward substitutions and residual evaluations, respectively.

case, while an in-house code was developed for both Leja adaptive algorithms [37]. We compare the resulting surrogate models with respect to accuracy and computational costs.

The computational costs refer to the number of model evaluations needed for the approximation’s construction. While straightforward for the gPC and the Leja adaptive Algorithm 1, the estimation of costs is more involved in the case of the adjoint-based Algorithm 2. First, in order to evaluate the duality-based error indicator (68) at a candidate point, it is sufficient to evaluate a residual of (31). Therefore, we distinguish between residual evaluations and solver calls, where in most cases the costs to evaluate the residuals are almost negligible compared to the solver costs, i.e. assembly and sparse LU decomposition of the system matrices $\mathbf{A}_{\text{dof}}(\mathbf{y})$. Second, the additional costs for computing the dual solution \mathbf{z} by forward and backward substitution can also be neglected in most cases, since the primal problem is solved with a sparse LU decomposition.

The accuracy of the surrogate models is measured using a validation set of $N^{\text{MC}} = 5000$ parameter realizations $S^{(i)} := S(\mathbf{y}^{(i)})$, $i = 1, \dots, N^{\text{MC}}$, drawn according to the underlying PDF. We compute a discrete approximation of the L^1_q error

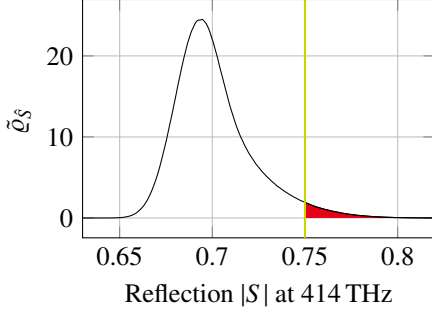
$$\mathbb{E}[|S - \tilde{S}|] \approx \frac{1}{N^{\text{MC}}} \sum_{i=1}^{N^{\text{MC}}} |S^{(i)} - \tilde{S}^{(i)}|. \quad (76)$$

Additionally, we also consider the maximum error over all samples

$$\max_{i=1, \dots, N^{\text{MC}}} |S^{(i)} - \tilde{S}^{(i)}|. \quad (77)$$

To obtain a better approximation of the maximum error, i.e. to take into account the low-probability “tails” of the RVs’ PDFs, we generate an additional cross-validation set of 5000 samples, for which the RVs are uniformly distributed in the corresponding ranges.

All accuracy and cost results are presented in Table 3. First, a gPC approximation with a 2nd order total-degree polynomial basis, i.e. 171 Jacobi polynomials, is constructed. The polynomial coefficients are computed with a sparse 2nd order Gauss quadrature formula, resulting in 613 quadrature nodes, accordingly, model evaluations. We set a budget $B = 613$ for the classic, i.e. without adjoints, Leja adaptive Algorithm 1, such that its costs are identical to the gPC. As can be seen in Table 3, the Leja adaptive approximation is at least one order of magnitude more accurate than the gPC, for both error metrics. For the adjoint-based Algorithm 2, we first compute an approximation using again 613 polynomials, resulting in errors almost identical to the non-adjoint case. However, since the costs can be predominantly attributed to the 421 solver calls, the costs are reduced by almost a third. We note that, in this case, both Leja adaptive approximations, i.e. with and without adjoint error indicators, employ the same multi-index set Λ , albeit slightly permuted. It is also worth noting that the polynomial surrogate models are not necessarily completely identical, since, on the one hand, the different ordering may lead to slightly different hierarchical surpluses s_ℓ and, on the other hand, after termination the classic Algorithm 1 uses the exact hierarchical surpluses s_ℓ for all $\ell \in \Lambda_+^{\text{adm}}$, while the adjoint-based Algorithm 2 uses the estimates \tilde{s}_ℓ instead. Next, we refine the adjoint-based approximation by employing (63) until 12000 polynomials are used, further reducing the error by more than one order of magnitude. As a reference, we also construct an approximation using 12000 polynomials with the *classic* Leja adaptive Algorithm 1. Both approximations achieve a very similar accuracy, however, the adjoint-based approach results in tremendous



(a) Estimated PDF of scattering parameter. Failure probability illustrated in red color.

N^{MC}	\mathbb{E}	$\sqrt{\mathbb{V}}$	\mathcal{F}
10^3	0.7007	0.0209	3.0%
10^4	0.7010	0.0206	2.9%
10^5	0.7009	0.0208	3.1%
10^6	0.7010	0.0209	3.1%
10^7	0.7010	0.0209	3.1%

(b) Expectation, standard deviation and failure probability, i.e. $\mathcal{F} = P(|S| \geq 1 - \alpha)$ for $\alpha = 0.25$. Surrogate-based Monte Carlo estimation using N^{MC} samples.

Figure 8: PDF, expectation, standard deviation and failure probability for 17 beta-distributed input parameters.

computational savings. It is worth noting that, in this particular case, the accuracy of the adjoint-based approximation is, by chance, slightly better. However, this cannot be expected in general.

As often pointed out in the literature, see e.g. [45], it is inefficient to reduce the stochastic error below the discretization error. Therefore, the stochastic approximation is not further refined and the most accurate surrogate model (Table 3, last row) is in the following used to compute statistical measures of the absolute value of the scattering parameter $|S|$.

4.2.1. Post-processing the sparse grid approximation

Since the polynomial surrogate model $\tilde{S}(\mathbf{y})$ can be evaluated inexpensively, we employ a Monte Carlo-based approach by evaluating the surrogate model on a large number of N^{MC} parameter samples, drawn from the joint PDF $\varrho(\mathbf{y})$. We then use the sample evaluations to estimate statistical moments of $|S|$, its PDF, failure probabilities based on specific design criteria, and its sensitivity with respect to the input parameters.

The expected value $\mathbb{E}[|S|]$ and the variance $\mathbb{V}[|S|]$ are estimated as

$$\mathbb{E}[|S|] = \int_{\Xi} |S(\mathbf{y})| \varrho(\mathbf{y}) \, d\mathbf{y} \approx \frac{1}{N^{\text{MC}}} \sum_{i=1}^{N^{\text{MC}}} |\tilde{S}^{(i)}|, \quad (78a)$$

$$\mathbb{V}[|S|] = \int_{\Xi} (|S(\mathbf{y})| - \mathbb{E}[|S|])^2 \varrho(\mathbf{y}) \, d\mathbf{y} \approx \frac{1}{N^{\text{MC}} - 1} \sum_{i=1}^{N^{\text{MC}}} (|\tilde{S}^{(i)}| - \mathbb{E}[|\tilde{S}|])^2. \quad (78b)$$

We estimate the failure probability $\mathcal{F} = P(|S| \geq 1 - \alpha)$ as

$$\mathcal{F} = P(|S| \geq 1 - \alpha) = \int_{S=1-\alpha}^{S=1} \varrho_S \, dS = \int_{\Xi} \mathcal{I}_{\mathcal{F}}(S(\mathbf{y})) \varrho(\mathbf{y}) \, d\mathbf{y} \approx \frac{1}{N^{\text{MC}}} \sum_{i=1}^{N^{\text{MC}}} \mathcal{I}_{\mathcal{F}}(\tilde{S}^{(i)}), \quad (79)$$

where ϱ_S denotes the PDF of $|S|$ and $\mathcal{I}_{\mathcal{F}}$ denotes the indicator function

$$\mathcal{I}_{\mathcal{F}}(S) = \begin{cases} 1, & |S| \in [1 - \alpha, 1], \\ 0, & |S| \in [0, 1 - \alpha). \end{cases}$$

Monte Carlo sampling in combination with surrogate modeling is used for simplicity here. However, it should be noted that equality in (79) for $N^{\text{MC}} \rightarrow \infty$ cannot be guaranteed in general, see [74] for counter-examples and possible extensions.

The PDF ϱ_S of $|S|$ is estimated by employing a kernel density estimator

$$\varrho_S \approx \tilde{\varrho}_T := \frac{1}{hN^{\text{MC}}} \sum_{i=1}^{N^{\text{MC}}} K\left(\frac{T - |\tilde{S}^{(i)}|}{h}\right) \quad (80)$$

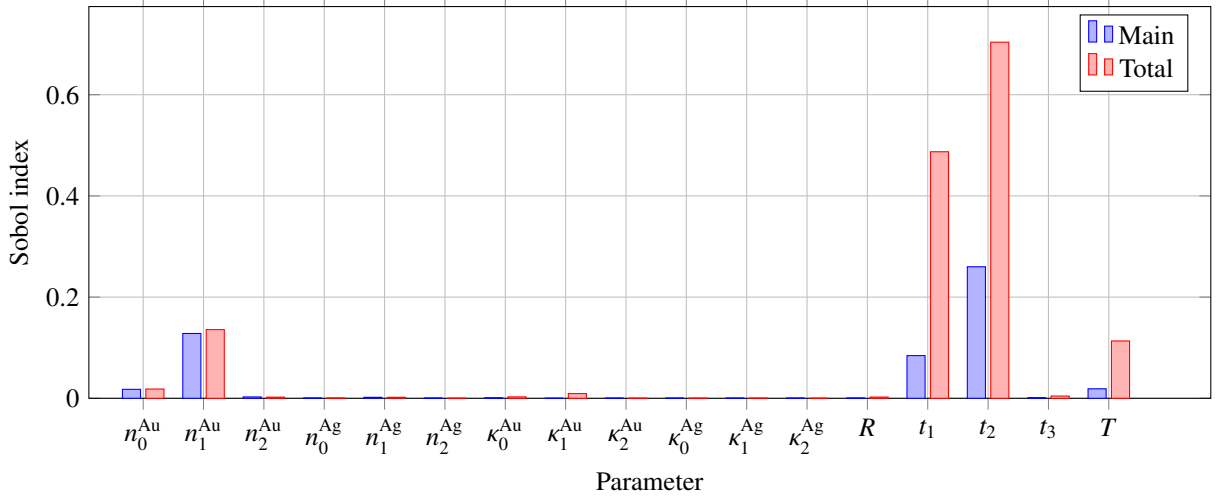


Figure 9: Sobol indices computed with 10^5 samples.

with $N^{\text{MC}} = 10^7$ samples, bandwidth $h = 10^{-3}$ and the Epanechnikov kernel [75]

$$K(T) := \begin{cases} \frac{3}{4}(1 - T^2), & T \in [-1, 1], \\ 0, & \text{else.} \end{cases}$$

The estimated expected values, standard deviations $\sqrt{\mathbb{V}}$ and failure probabilities for an increasing number of samples N^{MC} and $\alpha = 0.25$ are given in Table 8b. The estimated PDF \hat{q}_S is shown in Fig. 8a.

Sensitivity analysis is based on an analysis of variances (ANOVA) [76]. The related metrics are commonly known as Sobol indices, which can be computed directly from the gPC coefficients [77, 51]. We are interested in a sensitivity analysis for the magnitude of the scattering parameter. To this end, we first introduce a gPC approximation \hat{S} of $|S|$, where we again use the symbol $s_{\mathbf{p}}$ for the polynomial coefficients. Then, the variance can be computed as

$$\mathbb{V}[|S|] = \mathbb{E}[|S|^2] - \mathbb{E}[|S|]^2 \approx \sum_{0 < |\mathbf{p}| \leq p_{\max}} s_{\mathbf{p}}^2 \mathbb{E}[\Psi_{\mathbf{p}}^2] = \mathbb{V}[\hat{S}], \quad (81)$$

by exploiting the orthogonality property (35). Regarding the estimation of Sobol sensitivity indices, we will focus on the so-called main-effect (1st order) and total-effect (total order) indices. We define the multi-index sets $\Lambda_n^{\text{main}}, \Lambda_n^{\text{total}} \subset \Lambda_{p_{\max}}^{\text{TD}}$, $n = 1, 2, \dots, N$, such that

$$\Lambda_n^{\text{main}} = \{\mathbf{p} \in \Lambda_{p_{\max}}^{\text{TD}} : p_n \neq 0 \text{ and } p_m = 0, m \neq n\}, \quad \Lambda_{p_n}^{\text{total}} = \{\mathbf{p} \in \Lambda_{p_{\max}}^{\text{TD}} : p_n \neq 0\}. \quad (82)$$

We then define the partial variances $\mathbb{V}_n^{\text{main}}[\hat{S}]$ and $\mathbb{V}_n^{\text{total}}[\hat{S}]$, such that

$$\mathbb{V}_n^{\text{main}}[\hat{S}] := \sum_{\mathbf{p} \in \Lambda_n^{\text{main}}} s_{\mathbf{p}}^2 \mathbb{E}[\Psi_{\mathbf{p}}^2], \quad \mathbb{V}_n^{\text{total}}[\hat{S}] := \sum_{\mathbf{p} \in \Lambda_n^{\text{total}}} s_{\mathbf{p}}^2 \mathbb{E}[\Psi_{\mathbf{p}}^2]. \quad (83)$$

Then, the main-effect and total-effect Sobol indices, \hat{S}_n^{main} and \hat{S}_n^{total} , respectively, are given as

$$\hat{S}_n^{\text{main}} = \frac{\mathbb{V}_n^{\text{main}}[\hat{S}]}{\mathbb{V}[\hat{S}]}, \quad \hat{S}_n^{\text{total}} = \frac{\mathbb{V}_n^{\text{total}}[\hat{S}]}{\mathbb{V}[\hat{S}]}. \quad (84)$$

In the context of the present work, estimations of the Sobol indices (84) for the absolute value of the Leja approximation $\tilde{S} : \Xi \rightarrow \mathbb{C}$ shall be based on sampling of the polynomial approximation, since the corresponding polynomials do not fulfill the orthogonality condition (35). We use Saltelli's algorithm [78] with $N^{\text{MC}} = 10^5$ samples, resulting in $2(17 + 1)10^5 = 3.6 \times 10^6$ surrogate model evaluations. The main-effect and total-effect Sobol indices for each parameter are given in Fig. 9. The thickness of the upper gold layer t_1 , the thickness of the dielectric layer t_2 , the grating

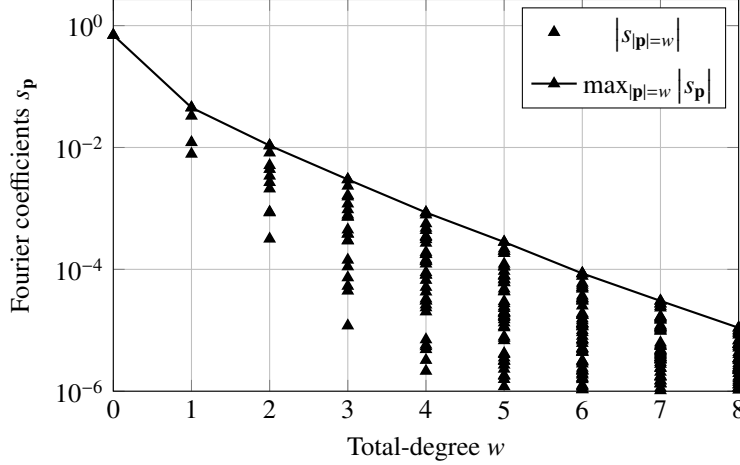


Figure 10: Decay of Fourier coefficients of the multivariate gPC approximation for the 4 most sensitive parameters.

depth T and the refractive index of the upper gold layer n_1^{Au} are identified as the most sensitive parameters. Moreover, since the sum of all main-effect sensitivity indices is approximately 52%, the remaining 48% indicates higher order interactions, and thus strong coupling among the input parameters.

It is found that the considered model is highly sensitive to small geometrical variations. In particular, while geometrical variations in a range of only ± 0.5 nm are considered, their impact is significantly higher than the one attributed to material uncertainty, which was modelled based on the measurement error provided by [65].

4.2.2. Decay of Fourier coefficients

We study the decay of polynomial coefficients to numerically investigate the smoothness of the mapping from the input parameters to the S-parameter and justify the use of polynomial approximations. It has been shown, see e.g. [79, Lemma 2] where Legendre polynomials are considered, that the Fourier coefficients $s_{\mathbf{p}}$ of an N -variate gPC approximation (37) decay exponentially, provided that the mapping is analytic. In particular, the estimate

$$|s_{\mathbf{p}}|^2 \leq C e^{-\sum_{n=1}^N g_n p_n}, \quad (85)$$

where C and g_n , $n = 1, \dots, N$ are positive constants independent of \mathbf{p} and where the polynomials are assumed to be normalized, i.e. $\mathbb{E}[\Psi_{\mathbf{p}} \Psi_{\mathbf{q}}] = \delta_{\mathbf{p}, \mathbf{q}}$, has been shown. We consider the maximum of the absolute value of the Fourier coefficients $s_{\mathbf{p}}$ with fixed total-degree w

$$\max_{|\mathbf{p}|=w} |s_{\mathbf{p}}|^2 \leq \max_{|\mathbf{p}|=w} C e^{-\sum_{n=1}^N g_n p_n} = C e^{-\min_{|\mathbf{p}|=w} \sum_{n=1}^N g_n p_n} \leq C e^{-(\min_n g_n)w}. \quad (86)$$

It can be seen that the maximum Fourier coefficient is expected to decay exponentially with an increasing total-degree w .

Based on the sensitivity analysis results in Table 2, we restrict input uncertainties to the 4 most sensitive parameters, i.e. t_1 , t_2 , T , and n_1^{Au} , and construct a gPC approximation with a total-degree $p_{\text{max}} = 8$ polynomial basis. The multivariate integrals of the pseudo-spectral projection (38) are computed by a Gauss quadrature of the same order. All coefficients $s_{\mathbf{p}}$ are plotted in Fig. 10, where an exponential decay can indeed be observed. This can be seen as a numerical indicator for smoothness of the approximated mapping $S(\mathbf{y})$.

4.3. Variable Frequency

In Section 4.2, the QoI was considered to be the scattering parameter at a fixed frequency. However, in many applications, one is interested in the uncertainty of the resonance in a given frequency range $[f_{\text{min}}, f_{\text{max}}]$, i.e.

$$S_{\text{res}}(\mathbf{y}) = \min_{f \in [f_{\text{min}}, f_{\text{max}}]} |S(f, \mathbf{y})|, \quad f_{\text{res}}(\mathbf{y}) = \arg \min_{f \in [f_{\text{min}}, f_{\text{max}}]} |S(f, \mathbf{y})|.$$

This poses an additional challenge in performing an efficient UQ. Indeed, the mathematical operations of computing the absolute value and the minimization are not in general differentiable with respect to the uncertain parameters.

	#LU	#FB	#Res	Max. Error (77)	Mean Error (76)
Isotropic Smolyak grid (level 2)	391	391	0	5.91×10^{-2}	1.67×10^{-2}
Adaptive Leja (without adjoints)	391	391	0	2.13×10^{-3}	4.08×10^{-4}
Adaptive Leja (with adjoints)	288	576	391	2.13×10^{-3}	4.09×10^{-4}
Adaptive Leja (without adjoints)	2000	2000	0	2.16×10^{-4}	3.94×10^{-5}
Adaptive Leja (with adjoints)	288	576	2000	2.14×10^{-4}	3.94×10^{-5}

Table 4: Accuracy and computational cost of different polynomial approximations for 13 input RVs. #LU refers to the dominating costs for the assembly and sparse LU decomposition of the system matrices. #FB and #Res denote the number of forward-backward substitutions and residual evaluations, respectively.

This is intuitively clear in the presence of more than one resonances inside the parameter range $[f_{\min}, f_{\max}]$ where the resonance frequency may jump from one resonance to another due to variations in the parameters. Since the convergence properties of polynomial approximations depend crucially on the smoothness of the mapping [24], polynomial approximations of the mappings $S_{\text{res}} : \Xi \rightarrow [0, 1]$, $f_{\text{res}} : \Xi \rightarrow [f_{\min}, f_{\max}]$ may not converge.

To circumvent this issue, we propose the following workflow: first, we create a polynomial surrogate $\tilde{S}(f, \mathbf{y})$ of $S : [f_{\min}, f_{\max}] \times \Xi \rightarrow \mathbb{C}$. Since the polynomial surrogate can be evaluated inexpensively, we then calculate all statistical measures by Monte Carlo estimators which only require square-integrability. In particular, we draw N^{MC} samples of the input RVs \mathbf{Y} and evaluate for each sample $\mathbf{y}^{(i)}$ the resonance $\tilde{S}_{\text{res}}(\mathbf{y})$ and resonance frequency $\tilde{f}_{\text{res}}(\mathbf{y})$, by solving the minimization problem for a univariate polynomial

$$\tilde{S}_{\text{res}}^{(i)} := \tilde{S}_{\text{res}}(\mathbf{y}^{(i)}) = \min_{f \in [f_{\min}, f_{\max}]} |\tilde{S}(f, \mathbf{y}^{(i)})|, \quad \tilde{f}_{\text{res}}^{(i)} := \tilde{f}_{\text{res}}(\mathbf{y}^{(i)}) = \arg \min_{f \in [f_{\min}, f_{\max}]} |\tilde{S}(f, \mathbf{y}^{(i)})|. \quad (87)$$

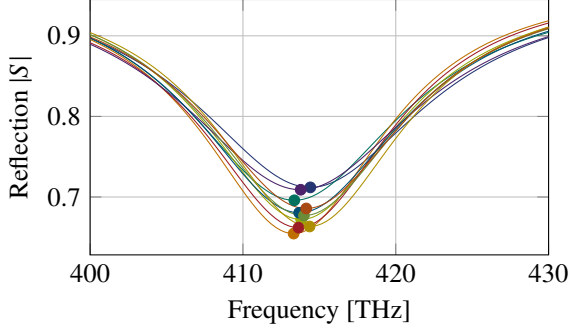
All statistical measures, e.g. expected values, variances, sensitivity indices, failure probabilities and quantiles, can then be computed from the samples $\{\tilde{S}_{\text{res}}^{(i)}\}_{i=1}^{N^{\text{MC}}}$, $\{\tilde{f}_{\text{res}}^{(i)}\}_{i=1}^{N^{\text{MC}}}$.

We apply the described UQ workflow for the resonance of scattering parameters of the optical grating coupler in a narrow frequency range. In this subsection we exclude geometrical uncertainty such that only the 12 uncertain material parameters given in Table 1 are considered, for which at least a rough estimate of the uncertainty magnitude is available from measurements. We model them as uniformly distributed in the ranges defined by nominal value \pm variation. In this way, we can easily compare the results to an isotropic Smolyak approach, which is often formulated for uniform random variables. Moreover, considering uniform distributions for the adaptive collocation method is reasonable in general, as accurate tail approximations can be obtained in this way. The true, possibly non-uniform, distribution can still be taken into account afterwards using a suitable random number generator for sampling the surrogate model.

Following the aforementioned workflow, we first create a surrogate model for the scattering parameter $S : [f_{\min}, f_{\max}] \times \Xi \rightarrow \mathbb{C}$, where \mathbf{y} now corresponds to the 12 parameters $n_i^{\text{Au}}, \kappa_i^{\text{Au}}, n_i^{\text{Ag}}, \kappa_i^{\text{Ag}}$, $i = 0, 1, 2$. We apply the adaptive Leja Algorithms 1 and 2 to construct polynomial approximations of the numerical model $\tilde{S}(f, \mathbf{y})$. As in the single frequency case, we employ the error metrics (77) and (76) on a cross-validation set of $N^{\text{MC}} = 10^3$ samples. Results are given in Table 4. We additionally construct an isotropic Smolyak sparse-grid of level 2 [80] using Gauss-Legendre nodes for the 13-dimensional parameter space $[f_{\min}, f_{\max}] \times \Xi$. Comparing the isotropic sparse grid approximation to the dimension-adaptive one, the latter is found to be clearly superior in terms of accuracy. Exploiting the adjoint error indicator (68) either increases the accuracy or decreases the computational costs further. Finally, we obtain a very accurate surrogate model using 2000 polynomials and only 288 sparse LU decompositions. Cross-validation indicates that the parametric error is below the FE discretization error.

Using the accurate polynomial model $\tilde{S}(f, \mathbf{y}^{(i)})$ (Table 4, last row), we perform UQ for the resonance (87). After drawing $N^{\text{MC}} = 10^6$ samples $\{\mathbf{y}^{(i)}\}_{i=1}^{N^{\text{MC}}}$ from the joint PDF, we obtain N^{MC} univariate polynomials $\tilde{S} : [f_{\min}, f_{\max}] \rightarrow \mathbb{C}$. For each polynomial, we solve the minimization problem (87) using SQP [71, Chapter 18]. In order to ensure that the global minimum is found, one can restart the algorithm with different initial values. For this particular model, $n_{\text{init}} = 3$ different initial values at {400, 415, 430} THz are used.

As an illustration, Fig. 11a shows the frequency response and the resonance frequency for 10 random samples of the input parameters. Table 11b presents expected values and standard deviations for the resonance frequency f_{res} , as well as the corresponding S-parameter value $|S_{\text{res}}|$. Additionally, we estimate the failure probability $\mathcal{F}_{\text{res}} = P(|S_{\text{res}}| \geq 0.7)$. All results are computed using Monte Carlo estimators with $N^{\text{MC}} = 10^6$ samples of the surrogate model. The results underline that the uncertainty in the measured optical constants of noble metals affects the computed outputs.



(a) Frequency response for 10 random parameter samples $\mathbf{y}^{(i)}$. Dots illustrate resonances.

	\mathbb{E}	$\sqrt{\mathbb{V}}$	\mathcal{F}_{res}
$ S_{\text{res}} $	0.685	0.017	21.9%
f_{res} [THz]	413.827	0.324	–

(b) Expectation, standard deviation and failure probability, i.e. $\mathcal{F}_{\text{res}} = P(|S_{\text{res}}| \geq 0.7)$.

Figure 11: UQ for the resonance of the scattering parameter in a narrow frequency range.

5. Conclusion

In this work we presented an efficient method to quantify uncertainties of the scattering parameter, assuming a moderately large number of input RVs. Dimension adaptivity in combination with an adjoint-error indicator are confirmed to be a promising technique to delay the curse-of-dimensionality. For the considered FE model of an optical grating coupler, the comparison of the proposed Leja algorithm with total degree gPC and isotropic Smolyak sparse grids shows significant gains in both accuracy and computational costs. In particular, with the adaptive scheme we were able to consider up to 17 parameters and achieve an accuracy of $\approx 10^{-3}$ with less than 500 model evaluations.

In order to perform efficient UQ for the resonance of frequency-dependent scattering parameters, a polynomial surrogate model was created by treating the excitation frequency as an additional parameter. Exploiting that the surrogate model can be inexpensively evaluated, all statistical measures were then calculated by Monte Carlo estimators which only require square integrability. It was further observed that, in the multivariate case, the maximum of the Fourier coefficients with fixed total degree, decays exponentially. This indicates smoothness of the output with respect to the input parameters and underlines that polynomial approximations are well-suited for this model, at least for moderate sizes of the parameter variability and frequency range. To consider wider frequency ranges with possible poles in combination with large geometric uncertainties, a combination of polynomial and rational approximations is a topic of future research.

For the considered optical grating coupler, according to Sobol-sensitivity measures, geometrical parameters have been found to be the dominant source of input uncertainty. Although the modeling of their probability distributions could not be based on measurement data yet, this conclusion is substantiated by the very conservative choice of geometrical standard deviations.

Acknowledgments

The authors would like to thank R. Schuhmann for valuable discussions on the the topic of UQ in plasmonics, in particular for pointing out relevant quantities to compute. The work of N. Georg, D. Loukrezis and S. Schöps is supported by the *Excellence Initiative* of the German Federal and State Governments and the Graduate School of Computational Engineering at Technische Universität Darmstadt. N. Georg’s work is also funded by the DFG grant RO4937/1-1.

References

- [1] C. Genet, T. W. Ebbesen, Light in tiny holes, *Nature* 445 (2007) 39.
- [2] S. A. Maier, *Plasmonics: fundamentals and applications*, Springer Science & Business Media, New York, 2007.
- [3] B. S. Dennis, V. Aksyuk, M. I. Haftel, S. T. Koev, G. Blumberg, Enhanced coupling between light and surface plasmons by nano-structured fabry–perot resonator, *J. Appl. Phys.* 110 (2011) 066102.

- [4] J. Lu, C. Petre, E. Yablonovitch, J. Conway, Numerical optimization of a grating coupler for the efficient excitation of surface plasmons at an Ag-SiO₂ interface, *J. Opt. Soc. Am. B* 24 (2007) 2268.
- [5] M. J. Preiner, K. T. Shimizu, J. S. White, N. A. Melosh, Efficient optical coupling into metal-insulator-metal plasmon modes with subwavelength diffraction gratings, *Appl. Phys. Lett.* 92 (2008) 113109.
- [6] B. Gallinet, J. Butet, O. J. Martin, Numerical methods for nanophotonics: standard problems and future challenges, *Laser Photonics Rev.* 9 (2015) 577–603.
- [7] P. Lalanne, G. M. Morris, Highly improved convergence of the coupled-wave method for TM polarization, *J. Opt. Soc. Am. A* 13 (1996) 779–784.
- [8] G. Granet, B. Guizal, Efficient implementation of the coupled-wave method for metallic lamellar gratings in TM polarization, *J. Opt. Soc. Am. A* 13 (1996) 1019–1023.
- [9] K. S. Kunz, R. J. Luebbers, *The finite difference time domain method for electromagnetics*, CRC press, Boca Raton, 1993.
- [10] T. Weiland, Time domain electromagnetic field computation with finite difference methods, *Int. J. Numer. Model. Electron. Network. Dev. Field* 9 (1996) 295–319.
- [11] A. Taflove, S. C. Hagness, *Computational electrodynamics: the finite-difference time-domain method*, Artech house, Norwood, 2005.
- [12] F. G. De Abajo, J. Aizpurua, Numerical simulation of electron energy loss near inhomogeneous dielectrics, *Phys. Rev. B* 56 (1997) 15873.
- [13] J. Waxenegger, A. Trügler, U. Hohenester, Plasmonics simulations with the MNPBEM toolbox: Consideration of substrates and layer structures, *Comput. Phys. Commun.* 193 (2015) 138–150.
- [14] J.-M. Jin, *The Finite Element Method in Electromagnetics*, John Wiley & Sons, Hoboken, 2015.
- [15] P. Monk, *Finite element methods for Maxwell’s equations*, Oxford University Press, 2003.
- [16] C. Chauviere, J. S. Hesthaven, L. Lurati, Computational modeling of uncertainty in time-domain electromagnetics, *SIAM J. Sci. Comput.* 28 (2006) 751–775.
- [17] J. Niegemann, M. König, K. Stannigel, K. Busch, Higher-order time-domain methods for the analysis of nanophotonic systems, *Photonics Nanostructures: Fundam. Appl.* 7 (2009) 2–11.
- [18] K. Busch, M. König, J. Niegemann, Discontinuous Galerkin methods in nanophotonics, *Laser Photonics Rev.* 5 (2011) 773–809.
- [19] N. Schmitt, C. Scheid, S. Lanteri, A. Moreau, J. Viquerat, A DGTD method for the numerical modeling of the interaction of light with nanometer scale metallic structures taking into account non-local dispersion effects, *J. Comput. Phys.* 316 (2016) 396 – 415.
- [20] N. Schmitt, C. Scheid, J. Viquerat, S. Lanteri, Simulation of three-dimensional nanoscale light interaction with spatially dispersive metals using a high order curvilinear DGTD method, *J. Comput. Phys.* (2018). Accepted.
- [21] D. Xiu, Fast numerical methods for stochastic computations: A review, *Commun. Comput. Phys.* 5 (2009) 242–272.
- [22] R. G. Ghanem, P. D. Spanos, *Stochastic Finite Elements: A Spectral Approach*, Springer, New York, 1991.
- [23] I. Babuska, R. Tempone, G. E. Zouraris, Galerkin finite element approximations of stochastic elliptic partial differential equations, *SIAM J. Numerical Analysis* 42 (2004) 800–825.
- [24] I. Babuska, F. Nobile, R. Tempone, A stochastic collocation method for elliptic partial differential equations with random input data, *SIAM Review* 2 (2010) 317–355.

- [25] D. Xiu, G. E. Karniadakis, The Wiener-Askey polynomial chaos for stochastic differential equations, *SIAM J. Scientific Computing* 24 (2002) 619–644.
- [26] D. Xiu, J. S. Hesthaven, High-order collocation methods for differential equations with random inputs, *SIAM J. Scientific Computing* 27 (2005) 1118–1139.
- [27] W. Hackbusch, Numerical tensor calculus, *Acta Numerica* 23 (2014) 651–742.
- [28] P. G. Constantine, *Active Subspaces: Emerging Ideas for Dimension Reduction in Parameter Studies*, Society for Industrial and Applied Mathematics, Philadelphia, 2015.
- [29] T. Wittig, R. Schuhmann, T. Weiland, Model order reduction for large systems in computational electromagnetics, *Linear Algebra Its Appl.* 415 (2006) 499–530.
- [30] P. Benner, J. Schneider, Uncertainty quantification for Maxwell’s equations using stochastic collocation and model order reduction, *Int. J. Uncertain. Quantif.* 5 (2015).
- [31] O. Farle, V. Hill, P. Nickel, R. Dyczij-Edlinger, Multivariate finite element model order reduction for permittivity or permeability estimation, *IEEE Trans. Magn.* 42 (2006) 623–626.
- [32] O. P. Le Maitre, O. M. Knio, *Spectral Methods for Uncertainty Quantification: With Applications to Computational Fluid Dynamics*, Scientific Computation, Springer Netherlands, 2010.
- [33] P. Sochala, O. P. Le Maitre, Polynomial chaos expansion for subsurface flows with uncertain soil parameters, *Adv. Water Resour.* 62 (2013) 139 – 154.
- [34] G. Blatman, B. Sudret, An adaptive algorithm to build up sparse polynomial chaos expansions for stochastic finite element analysis, *Probailist. Eng. Mech.* 25 (2010) 183 – 197.
- [35] M. Motamed, F. Nobile, R. Tempone, A stochastic collocation method for the second order wave equation with a discontinuous random speed, *Numerische Mathematik* 123 (2013) 493–536.
- [36] A. C. M. Austin, C. D. Sarris, Efficient analysis of geometrical uncertainty in the fdtd method using polynomial chaos with application to microwave circuits, *IEEE Trans. Microw. Theory Tech.* 61 (2013) 4293–4301.
- [37] D. Loukrezis, U. Römer, H. De Gersem, Numerical Comparison of Leja and Clenshaw-Curtis Dimension-Adaptive Collocation for Stochastic Parametric Electromagnetic Field Problems, *ArXiv e-prints* (2017).
- [38] R. Hiptmair, L. Scarabosio, C. Schillings, C. Schwab, Large deformation shape uncertainty quantification in acoustic scattering, *Adv. Comput. Math.* (2018) 1–44.
- [39] L. Scarabosio, Shape uncertainty quantification for scattering transmission problems, Ph.D. thesis, ETH Zurich, 2016.
- [40] A. Chkifa, A. Cohen, C. Schwab, High-dimensional adaptive sparse polynomial interpolation and applications to parametric pdes, *Found. Comput. Math.* 14 (2014) 601–633.
- [41] F. Bonizzoni, F. Nobile, I. Perugia, D. Pradovera, Least-Squares Padé approximation of parametric and stochastic Helmholtz maps, *ArXiv e-prints* (2018).
- [42] A. Narayan, J. D. Jakeman, Adaptive Leja sparse grid constructions for stochastic collocation and high-dimensional approximation, *SIAM J. Scientific Computing* 36 (2014).
- [43] T. Butler, P. Constantine, T. Wildey, A posteriori error analysis of parameterized linear systems using spectral methods, *SIAM J. Matrix Anal. Appl.* 33 (2012) 195–209.
- [44] T. Butler, C. Dawson, T. Wildey, Propagation of uncertainties using improved surrogate models, *SIAM/ASA J. Uncertainty Quantification* 1 (2013) 164–191.
- [45] J. D. Jakeman, T. Wildey, Enhancing adaptive sparse grid approximations and improving refinement strategies using adjoint-based a posteriori error estimates, *J. Comput. Physics* 280 (2015) 54–71.

- [46] B. Schieche, Unsteady Adaptive Stochastic Collocation on Sparse Grids, PhD Thesis, TU Darmstadt, 2012.
- [47] A. K. Bhattacharyya, Phased array antennas: Floquet analysis, synthesis, BFNs and active array systems, volume 179, John Wiley & Sons, Hoboken, 2006.
- [48] Y. Zhu, A. C. Cangellaris, Multigrid finite element methods for electromagnetic field modeling, volume 28, John Wiley & Sons, Hoboken, 2006.
- [49] J. C. Nedelec, Mixed finite elements in R^3 , *Numer. Math.* 35 (1980) 315–341.
- [50] D. Xiu, Numerical Methods for Stochastic Computations: A Spectral Method Approach, Princeton University Press, Princeton, 2010.
- [51] G. Blatman, B. Sudret, Adaptive sparse polynomial chaos expansion based on least angle regression, *J. Comput. Physics* 230 (2011) 2345–2367.
- [52] B. J. Deusschere, H. N. Najm, P. P. Pébay, O. M. Knio, R. G. Ghanem, O. P. Le Maitre, Numerical challenges in the use of polynomial chaos representations for stochastic processes, *SIAM J. Scientific Computing* 26 (2004) 698–719.
- [53] O. P. Le Maitre, O. M. Knio, H. N. Najm, R. G. Ghanem, A stochastic projection method for fluid flow: I. basic formulation, *J. Comput. Physics* 173 (2001) 481–511.
- [54] G. Migliorati, F. Nobile, E. von Schwerin, R. Tempone, Analysis of discrete L2 projection on polynomial spaces with random evaluations, *Found. Comput. Math.* 14 (2014) 419–456.
- [55] V. Barthelmann, E. Novak, K. Ritter, High dimensional polynomial interpolation on sparse grids, *Adv. Comput. Math.* 12 (2000) 273–288.
- [56] H.-J. Bungartz, M. Griebel, Sparse grids, *Acta Numerica* 13 (2004) 147–269.
- [57] A. Klimke, B. I. Wohlmuth, Algorithm 847: Spinterp: Piecewise multilinear hierarchical sparse grid interpolation in MATLAB, *ACM Trans. Math. Softw.* 31 (2005) 561–579.
- [58] F. Nobile, R. Tempone, C. G. Webster, A sparse grid stochastic collocation method for partial differential equations with random input data, *SIAM J. Numerical Analysis* 46 (2008) 2309–2345.
- [59] S. A. Smolyak, Quadrature and interpolation formulas for tensor products of certain classes of functions, *Dokl. Acad. Nauk SSSR* 4 (1963) 240–243.
- [60] T. Gerstner, M. Griebel, Dimension-adaptive tensor-product quadrature, *Computing* 71 (2003) 65–87.
- [61] R. Becker, R. Rannacher, An optimal control approach to a posteriori error estimation in finite element methods, *Acta Numerica* 10 (2001) 1–102.
- [62] U. Römer, S. Schöps, Adjoint error estimation for a pseudo-spectral approach to stochastic field-circuit coupled problems, in: *Proc. Appl. Math. Mech.*, volume 15, Wiley-VCH, 2015, pp. 711–714. doi:10.1002/pamm.201510345.
- [63] A. L. Teckentrup, R. Scheichl, M. B. Giles, E. Ullmann, Further analysis of multilevel monte carlo methods for elliptic PDEs with random coefficients, *Numer. Math.* 125 (2013) 569–600.
- [64] CST AG, Optical applications with CST Microwave Studio, 2012. https://www.cst.com/content/events/downloads/euc2012/talk_5-3-1_cst_euc_2012.pdf (Accessed: 2018-03-12).
- [65] P. B. Johnson, R.-W. Christy, Optical constants of the noble metals, *Physical review B* 6 (1972) 4370.
- [66] C. Geuzaine, J.-F. Remacle, Gmsh: A 3-D finite element mesh generator with built-in pre-and post-processing facilities, *Int. J. Numer. Meth. Eng.* 79 (2009) 1309–1331.
- [67] M. Alnæs, J. Blechta, J. Hake, A. Johansson, B. Kehlet, A. Logg, C. Richardson, J. Ring, M. E. Rognes, G. N. Wells, The FEniCS project version 1.5, *Archive of Numerical Software* 3 (2015) 9–23.

- [68] CST AG, CST STUDIO SUITE 2016, 2018. URL: <https://www.cst.com>.
- [69] V. Braibant, C. Fleury, Shape optimal design using B-splines, *Comput. Methods Appl. Mech. Eng.* 44 (1984) 247–267.
- [70] L. Piegl, W. Tiller, *The NURBS Book*, 2 ed., Springer, 1997.
- [71] J. Nocedal, S. J. Wright, *Numerical optimization*, Springer Series in Operations Research and Financial Engineering, 2nd ed., Springer, New York, 2006.
- [72] R. H. Lopes, Kolmogorov-Smirnov test, in: *International Encyclopedia of Statistical Science*, Springer, 2011, pp. 718–720.
- [73] J. Feinberg, H. P. Langtangen, Chaospy: An open source tool for designing methods of uncertainty quantification, *J. Comput. Science* 11 (2015) 46–57.
- [74] J. Li, D. Xiu, Evaluation of failure probability via surrogate models, *J. Comput. Phys.* 229 (2010) 8966–8980.
- [75] V. A. Epanechnikov, Non-parametric estimation of a multivariate probability density, *Theor. Probab. Appl.* 14 (1969) 153–158.
- [76] I. M. Sobol, Global sensitivity indices for nonlinear mathematical models and their Monte Carlo estimates, *Math. Comput. Simul.* 55 (2001) 271 – 280.
- [77] G. Blatman, *Adaptive Sparse Polynomial Chaos Expansions for Uncertainty Propagation and Sensitivity Analysis*, Ph.D. thesis, Université Blaise Pascal, Clermont-Ferrand, France, 2009.
- [78] A. Saltelli, Making best use of model evaluations to compute sensitivity indices, *Comput. Phys. Commun.* 145 (2002) 280–297.
- [79] F. Nobile, R. Tempone, Analysis and implementation issues for the numerical approximation of parabolic equations with random coefficients, *Int. J. Numer. Meth. Eng.* 80 (2009) 979–1006.
- [80] J. Bäck, F. Nobile, L. Tamellini, R. Tempone, Stochastic spectral Galerkin and collocation methods for PDEs with random coefficients: a numerical comparison, in: J. Hesthaven, E. Ronquist (Eds.), *Spectral and High Order Methods for Partial Differential Equations*, volume 76 of *Lecture Notes in Computational Science and Engineering*, Springer, 2011, pp. 43–62. Selected papers from the ICOSAHOM '09 conference, June 22-26, Trondheim, Norway.